EXCLUSIVE PHOTOPRODUCTION OF ψ(2S) IN ELECTRON-PROTON COLLISION AT HERA

ZULIDZA BINTI ZULKAPLY

FACULTY OF SCIENCE
UNIVERSITY OF MALAYA
KUALA LUMPUR

2012

EXCLUSIVE PHOTOPRODUCTION OF ψ(2S) IN ELECTRON-PROTON COLLISION AT HERA

ZULIDZA BINTI ZULKAPLY

DISSERTATION SUBMITTED IN FULFILMENT OF THE REQUIREMENT FOR THE DEGREE OF MASTER OF SCIENCE

DEPARTMENT OF PHYSICS
FACULTY OF SCIENCE
UNIVERSITY OF MALAYA
KUALA LUMPUR

2012

ABSTRACT

The exclusive photoproduction of $\psi(2S)$ mesons, γp $\psi' p$, has been studied in electron-proton collisions with the ZEUS detector at HERA, in the kinematic range of $30<W<170$ GeV, where W is the photon-proton centre-of-mass energy. The $\psi(2S)$ was reconstructed in the $J/\psi\pi^+\pi^-$ decay channel where J/ψ was detected using the muon decay channel. The events data were taken from year 2003 to 2007 with the integrated luminosity of 354.18pb^{-1}. The negative four-momentum squared of exchange photon, Q^2 were taken to be less than 1 GeV as the scattered electron remained undetected down the beampipe.

ABSTRAK

Pengeluaran dari photon bagi zarah meson $\psi(2S)$ secara ekslusif, $\gamma p \quad \psi' p$ telah dikaji dalam pelanggaran electron-proton menggunakan detector ZEUS di HERA, dalam julat kinematik 30<W<170 GeV, dimana W adalah pusat-jisim tenaga bagi photon-proton. Zarah $\psi(2S)$ dibina dalam saluran reputan $J/\psi\pi^{+}\pi^{-}$ yang mana J/ψ pula dikesan menggunakan saluran reputan muon. Data peristiwa diambil dari tahun 2003 sehingga 2007 dengan sinaran integrasi 354.18pb^{-1}. Empat-momentum kuasa dua negatif bagi pertukaran photon, Q^2 dianggap kurang dari 1 GeV memandangkan electron tersesar tidak dapat dikesan di dalam salur pancaran.

ACKNOWLEDGEMENT

First and foremost, thanks to Allah. I dedicate this thesis to my mother, Puan Saerah Bt Mohd Salleh, for her help, love and patience. Next, to my supervisor, Prof. Dr. Wan Ahmad Tajuddin Wan Abdullah, for all his guidance and patience. Not forgettable I dedicate this work to my former co-supervisor, Allahyarham Prof. Madya Dr. Burhanuddin Kamaluddin, ZEUS Collaboration members, UM Physics Department, ZEUSMal colleagues, all my family members, friends and everything inspired me. Last but not least, to Charlie. Thank you all.

TABLE OF CONTENTS

<u>Chapter 4: Tracking Effiency</u>

Chapter 5: Data Analysis and Results

LIST OF FIGURES

LIST OF TABLES

LIST OF SYMBOLS AND ABBREVIATIONS

Ψ’ / ψ (2S)	Psi particle
J/ ψ	J/psi particle
μ	Muon particle
π	Pi particle
2D	2-Dimensional
3D	3-Dimensional
BMUON	Barrel Muon Detector
BNL	Brookhaven National Laboratory
BRMUON	Barrel Rear Muon Detector
CAL	Calorimeter
CC	Charged Current
CTD	Central Tracking Detector
DESY	Deutch Elektronen Synchotron
DIS	Deep Inelastic Scattering
FMUON	Forward Muon
FTD	Forward Tracking Detector
GMUON	Global Muon System
GR	Grand Reprocess
HERA	Hadron Electron Ring Accelerator
MC	Monte Carlo
MIP	Minimum ionizing particle
MVD	Micro Vertex Detector
NC	Neutral Current
ORANGE	Overlying Routine Analysis of Ntuple Generation
PAW	Physics Analysis Workstation
PHP	Photoproduction

QCD	Quantum Chromodynamics
QED	Quantum Electrodynamics
RMUON	Rear Muon Detector
RTD	Rear Tracking Detector
SLAC	Stanford Linear Accelerator Center
SM	Standard Model
VM / VMs	Vector Meson / Vector Mesons
ZEVIS	Zeus Event Displays

CHAPTER 1

INTRODUCTION

1.1 **Photoproduction in Diffractive Scattering**

Photoproduction refers to particle production that originates from photon. The word photoproduction itself is rephrased from the word '*photon*' and '*production*'. The signature of exclusive photoproduction in electron-proton collision events strictly consists of only the decay products of the searched particle, with no other significant activity in other detector components, since the scattered electron and proton escape undetected down the beampipe at small angles portraying a diffractive scattering. Diffractive scattering is a process where the colliding particles scatter at a very small angles and have no connecting color flux in the final state. This involves a propagator carrying the vacuum quantum numbers, called the Pomeron [1] and described, in the soft regime, within the Regge theory . Figure 1.1 shows a schematic diagram of a photon emission in electron proton collision which subsequently produces a $\psi(2S)$ particle that decays to a J/ψ and a pion pair.

Since the first operation period in 1992, ZEUS and H1, the two experiments dedicated to the deep inelastic scattering (DIS) physics at Hadron Electron Ring Accelerator (HERA), observed that approximately about 10% of lepton-proton DIS events had a diffractive origin. It opens a new area of studies in particle production mechanism including the photoproduction events , providing a hard scale which can be varied over a wide range and therefore it is an ideal testing ground for Quantum Chromodynamics (QCD) models. Diffractive production of Vector Mesons (VMs) and real photons, γ, allows studies on the transition from the soft to the hard regime in strong interactions. The hard regime (high energy and low Bjorken-x, x_{Bj}) is sensitive to the gluon content and well described by perturbative-QCD, while in the soft regime (low-x) the interaction is well described within the Regge phenomenology. The diffractive production of real photons, a process known as Deeply Virtual Compton Scattering (DVCS), leads to the extraction of the Generalized Parton Distribution functions (GPDs), containing combined information about the longitudinal momentum distribution of partons and their position on the transfer plane. The GPD-based calculations will be very helpful in the description of the Higgs boson diffractive production mechanism, which will be experimentally studied with the Large Hadron Collider (LHC) accelerator.

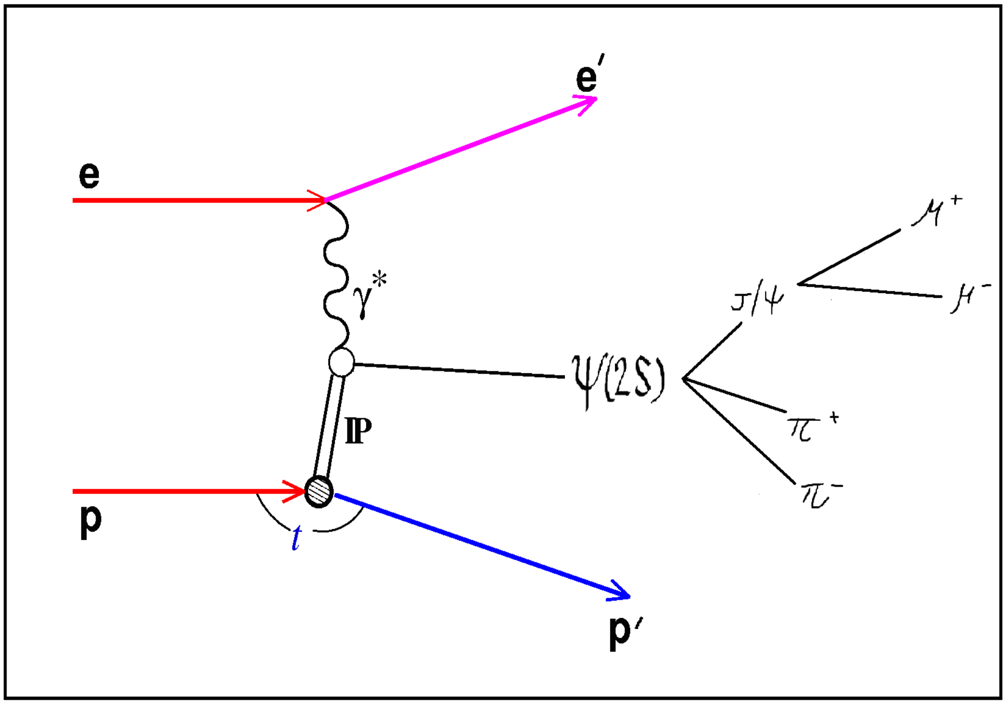

Figure 1.1: The picture shows the schematic diagram of $\psi(2S)$ photoproduction in electron-proton collision where the scattered electron and proton escape undetected in the beampipe.

1.2 The Standard Model

For many years, the development of particle physics research has been of huge interest for the physicists in exploring the quantum field theory. Beginning with the establishment of the basic particle foundation in the Standard Model (SM) as illustrated in Figure 1.2, the journey of particle search had changed rapidly through the subsequent years. Although it was strongly suggested that there are only three generations of fundamental particles according to SM, the latest and highest energy of collider, LHC is giving hope for the discovery of the new neutral current (NC) which has yet to be discovered, Higgs boson.

The history of the SM begins in early 1964, when the idea and discovery of quarks had extended the major believe of basic theory of structures of atoms and nuclei. In the era when scientists had put the quark as just a mathematical concept, the thinking had grown to the higher level of determining the real existence of these invisible partons or quarks. Rapidly developing research since then proved that their hard work was rewardable as they constantly managed to put on more facts of the quarks. In 1967, Weinberg and Salam had came out with the idea of unifying electromagnetic and weak interaction into electroweak interaction which required the existence of a neutral boson Z^0. Until three years later, Glashow, Ilioponlos and Maiani had recognized that the critical importance of the charm quark had allowed the theory of Z^0-mediated in weak interaction. This research of Z^0 weak force boson had continuously done until it was observed in 1973 by Andre Lagarrigue and his collaboration as the neutral manifestation of the weak force which had been predicted by electroweak theory [2]. Along with the Z^0-exchange observation in late 1973, a quantum field theory of the strong interaction was formulated. It was similar in structure to quantum electrodynamic (QED) but involved colour charges, and named in quantum chromodynamics (QCD). The quark was determined to be a real particle with colour charge and the gluon as the massless quantum of the strong interaction field. Also in the same year, Politzer, Gross and Wilczek, predefined the colour theory of the strong force which then introduced a new property called the asymptotic freedom.

In 1974, it was the first time J/ψ was discovered by two separate research groups, led respectively by Ting from the Brookhaven National Laboratory (BNL) and Richter from the Stanford Linear Accelerator Center (SLAC) [3]. This discovery had widened the understanding of the charmonium particles or charm-anticharm bound-state quarks which were singularly discovered earlier. Not long after the first discovery, the Richter's group again discovered the first excited state of the J/ψ which was known as ψ' or $\psi(2S)$, or occasionally $\psi(3686)$, indicating its quatum state or mass in MeV/c^2. The J/ψ family production was identified as one of the most popular particle research done in high energy physics experiments. The popularity is attributable to the high efficiency of this particle to be seen in the experiment. Figure 1.3 shows the journey of the SM history together with the initial particle discoveries.

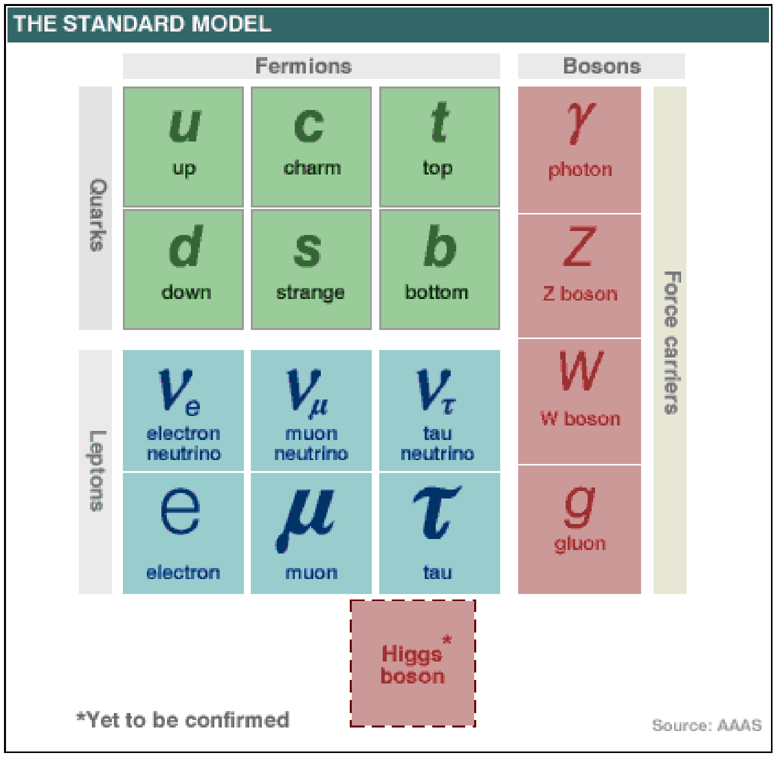

Figure 1.2: The diagram of the Standard Model (SM) of elementary particles

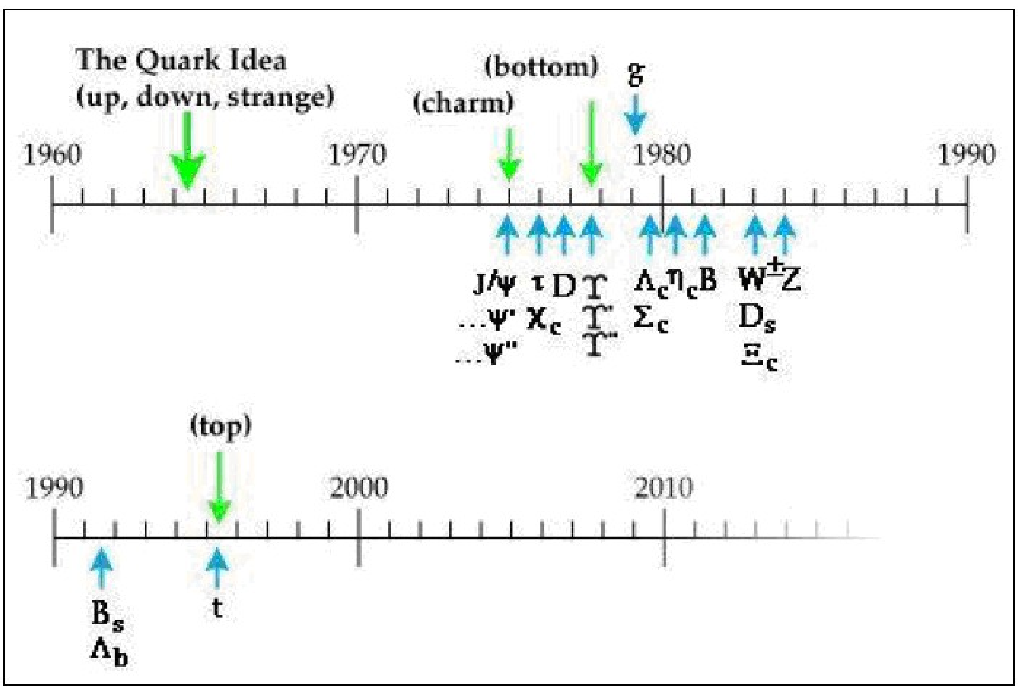

Figure 1.3: The Standard Model development in historical perspective. The idea of quarks as the constituents of matter and their subsequent experimental confirmation are shown.

1.3 Thesis Overview

In this thesis, we are going to study the exclusive photoproduction (PHP) of the first exited state of J/ψ, ψ' or $\psi(2S)$ with the rest-mass frame of 3686.093 ± 0.034 MeV/c^2 at the electron-proton collider, HERA located at Deutch Elektronen Syncrothron (DESY), Hamburg, Germany. At HERA, a proton beam of energy 920 GeV collides with an electron or positron beam of energy 27.52 GeV. The interaction between proton and electron will produce the exchange of specific gauge bosons depending on the interaction force whether it be electromagnetic, weak or strong. For weak interaction, the exchange gauge boson is either a charged current (CC), $W^{\pm}$ or neutral current (NC), Z^0. While for the strong and electromagnetic (EM) forces, the exchange boson will be a gluon (g) and a photon (γ) respectively. The significant and interesting features of learning this heavy vector meson (VM) production is one unique characteristics of the daughter products, which is the the combination of hadronic particles, in diffractive interaction. In the search for $\psi(2S)$, we are combining J/ψ (which decays to a muon pair) and a pion pair which are exclusively produced at the primary vertex of the electron-proton collisions. Muons, are prevalently known as minimum ionizing particles (MIP), will behave consistently stable through the detector's inner components such as the calorimeter, giving a special signature in the form of free isolated trajectory tracks. This muon will be subsequently

---

[1] In the following, for simplicity we will denote the charged lepton as electron, independently wether it is an e^+ or an e^-, unless otherwise stated

detected at the specific surface component called the Muon Detector. In contrast, pions will be detected rapidly near the interaction area in the Central Tracking Detector (CTD). The particle properties of these muons of J/ψ and pion pair will be useful for the study of the production cross-section of $\psi(2S)$. Moreover, the soft to hard transition of forces can be seen by studying the kinematics variables of the proton-photon interaction or typically known as W dependence of the cross-section for exclusive VM photoproduction.

The following is a brief preview of to upcoming chapters.

In Chapter 2, we shall go on to the kinematics of the electron-proton collision. Generally, the explanation in this chapter will focus on the process of exclusive photoproduction (PHP) at HERA which is the main subject matter in this thesis. In Chapter 3, there will be reviews of the experimental setup, the ZEUS Detector and HERA Accelerator. Meanwhile for Chapters 4, 5 and 6, the main discussion will focus on the tracking efficiency, $\psi(2S)$ production and results, and the conclusion, respectively. For the analytical method, in this study, we shall use open source software in the Linux Operating System, Physics Analysis Workstation or PAW which will be discussed further in Chapter 5.

CHAPTER 2

ELECTRON-PROTON COLLISION

2.1 Electron-proton collision at HERA

The collision between electron and proton at HERA is useful to obtain the kinematical values of particle diffraction and interaction at high energy. When an electron strikes a proton which contains quarks and gluons, the electron will transfer part of its energy and momentum to one of the quarks through the emission of a photon carrying a certain wavelength. The wavelength of the photon basically will reflect the strength of the interaction whether it is a hard or soft interaction. At HERA, the common phenomena observed are the diffractive interactions where the constituent quarks in the proton remain intact, $ep \rightarrow Xp$, where X is the new particle produced in the interaction. If the photon exchange between the electron and the proton only transfers a little momentum, the photon will only observe the main components of the proton which are the three individual valence quarks. However, if a greater momentum involve in the interaction, the HERA microscope will able to observe the quarks, anti-quarks and gluons in the proton. A photon-proton kinematics parameter called Q^2 is usually used to describe the strength of the momentum exchange. The Q^2 and the rest parameters will be explained in detail the next section. The force between the quarks can also be determined based on a coupling constant, α. An accurate measurement was taken at ZEUS have shown that, the coupling constant will increase with increasing distance. In quantum electrodynamics theory (QED), the energy scale of the interaction, $\mu^2 = Q^2$ thus, the following behaviour is observed:

$$\alpha(Q^2) = \frac{\alpha_0}{1 - \frac{\alpha_0}{3\pi}\ln\frac{Q^2}{m_e^2}} \tag{1}$$

where m_e^2 is the mass of electron, and α_0 is the coupling constant at $Q^2 = m_e^2$ [4]. In this thesis, α will be calculated to determine the photon flux in the cross section equation.

2.2 Kinematics of electron-proton (*ep*) scattering

The kinematic variables of *ep* scattering are the basic quantities used in ZEUS analysis to describe the scattering process of the collided particles. The schematic diagram for the *ep* scattering $e(k)p(P) \to e(k')X$ is shown in the Figure 2.1. Below are the relevant Lorentz invariant variables:

- $s = (k+P)^2$, the square of the centre-of-mass energy. At HERA, the centre-of-mass energy for *ep* is defined in the square root value of s, $\sqrt{s} = 318$ GeV.
- $Q^2 = -q^2 = -(k-k')^2$, the negative squared four-momentum of the exchanged virtual photon;

- $y = \frac{P.q}{P.k} = \frac{W^2}{s}$, the fraction of the positron energy transferred to the photon in the proton rest frame;
- $x_{Bj} = \frac{Q^2}{2(P.q)}$, the Bjorken variable, which can be interpreted as the fraction of the proton momentum carried by the struck charged parton;
- $W = (P+q)^2 = 2E_p(E-P_z)$, the squared centre-of-mass energy of the photon-proton system where E is the energy and P_z is the longitudinal momentum.

2.3 Diffraction

The diffraction at high energy describes processes in which the quantum numbers of the vacuum are exchanged. This physics phenomenon is also used as an alternative approach to the problem of perturbative and non-perturbative physics and the saturation of parton densities in the proton. Moreover, diffractive event is significantly useful for two pre-QCD phenomenological frameworks, Regge phenomenology and the Vector Dominance Model (VDM). The combination of the VDM and Regge phenomenology can be applied to describe certain physics processes, for example diffractive events at HERA. Generally there are three common diffractive processes in hadron-hadron collisions to be seen at HERA.

- Elastic scattering ($A+B \quad A+B$)

- Single diffraction ($A+B \quad B+X$)

- Double diffraction ($A+B \quad X+Y$)

Where the quantum numbers of X and Y are related to the incoming particles.

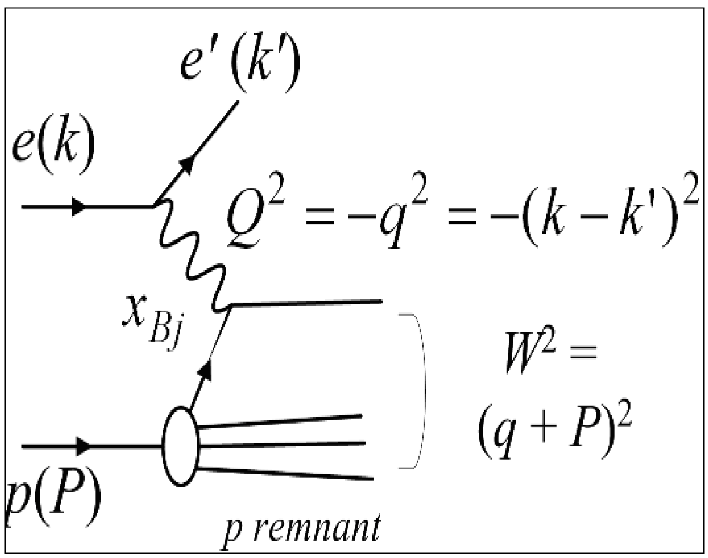

Figure 2.1: The picture shows a schematic diagram of *ep* scattering with the relevant kinematic variables.

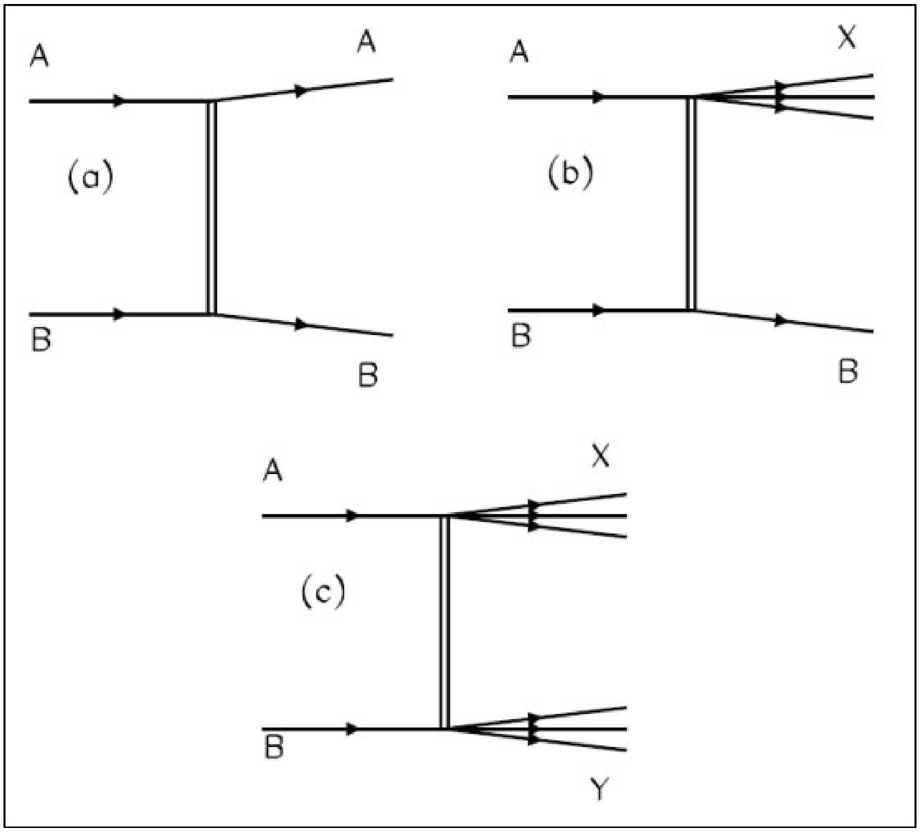

Figure 2.2: The classification of diffractive processes: (a) Elastic, (b) Single diffraction, (c) Double diffraction.

2.3.1 Regge Phenomenology

A simple spherically symmetric potential with discrete energy levels *k* and angular momentum *l* was defined in 1957 by Regge [5,6]. Then a complex value of *l* was recognized to obtain an interpolating function $a(l,k)$ which reduced to $a_l(k)$ for $l = 0,1,2,...$ n. The singularities of $a(l,k)$ turned out to be Regge poles [10] for Yukawa type potentials. It is located at values defined by a relation of the kind $l = \alpha(k)$ where $\alpha(k)$ is a function of the energy called the Regge trajectory. The Regge poles contributes to the scattering amplitude an asymptotically term (i.e for s and t fixed, where t is the four-momentum transfer between A and B) as

$$\lim(s \quad) A(s,t) \sim s^{\alpha(t)} \tag{2}$$

where $\alpha(t)$ is the Regge trajectory, assumed to be linear in t,

$$\alpha(t) = \alpha(0) + \alpha^{'} t \tag{3}$$

The intercept, $\alpha(0)$, and the slope, $\alpha^{'}$, of the trajectory are determined experimentally. The forward differential cross-section of the AB scattering is expressed by the following relations:

$$\frac{d\sigma_{el}}{dt}(t=0) \sim \frac{|A(s,t)|^2}{s^2} \sim e^{b(s)t}\left(\frac{s}{s_0}\right)^{2(\alpha(t)-1)} \tag{4}$$

where $b(s)$ is a parameters, which can be related to the transverse size of the interaction region similar to optical theorem,

$$\sigma_{AB \quad X} \sim \operatorname{Im} A(AB \quad AB, s, t = 0) \tag{5}$$

Hence the energy dependence of the total hadron-hadron cross-sections may be derived within the Regge theory (see Figure 2.3) and gives:

$$\sigma_{tot} \sim s^{\alpha(0)-1} \tag{6}$$

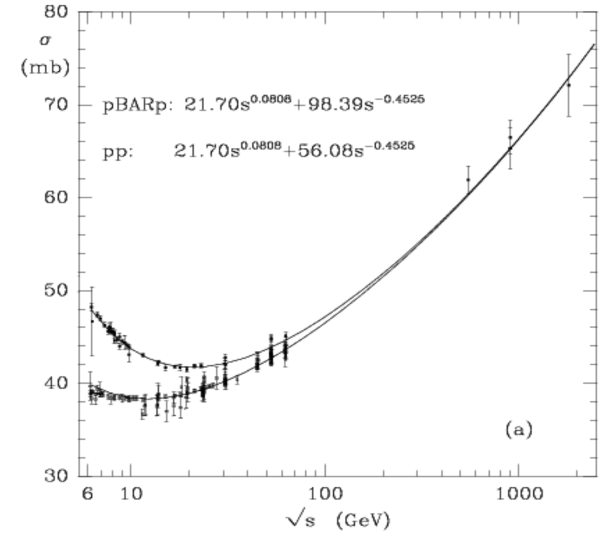

(a)

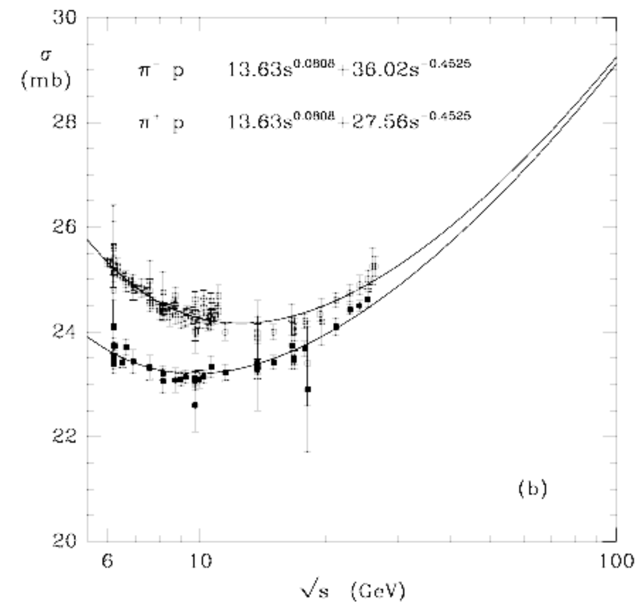

(b)

Figure 2.3: Total cross section measured in hadronic scattering as a function of centre-of-mass energy for (a) $pp, p\bar{p}$ and (b) $\pi \; p$ scattering. The total cross-sections drop at energy s < 10 GeV and increase consistently for higher energy level with the form of $\sigma \quad s^{0.08}$.

A global fit of hadron-hadron collisions was analysed by Donnachie and Lanshoff [7-9] to give the following relation,

$$\sigma_{tot} = Xs^{\alpha_R(0)-1} + Ys^{\alpha_P(0)-1} \tag{7}$$

where the first term corresponds to the exchange of all Reggeons dominating at low energies and the second terms accounts for the exchange Pomeron at high energies. Donnachie and Landshoff also performed fits to the |t| dependence of pp and $p\bar{p}$ cross sections following the parameterization. The result of the fits is given by the following trajectory:

$$\alpha_P(t) = 1.08 + 0.25t \tag{8}$$

where t is given in GeV/c^2, is often referred to as a Soft Pomeron.

2.3.2 Vector Dominance Model (VDM)

In VDM, a photon is a superposition of a QED photon and a hadronic component. This statement supports the appearance of a hadronic structure of the photon which was interpreted through the similarity of the measurement of the total cross section energy dependence in photon-hadron and hadron-hadron collisions. The hadronic component arises due to the quantum fluctuations ruled by the uncertainty principle. In the original VDM, the hadronic component is assumed to be a superposition of light vector mesons (VMs), which are ρ, ω and ϕ particles. In the Generalized VDM (GVDM) [11], when $Q^2 >> M_v^2$ (where M_v is the mass of a particular VMs) the higher mass states are included as well. In some events, the photon fluctuates into VM long before it interacts with the proton. In this case, a hadron-hadron type of interaction occurs between the VM and the proton. The similarity of energy dependence for hadron-hadron and photon-hadron interaction can be observed in Figure 2.4.

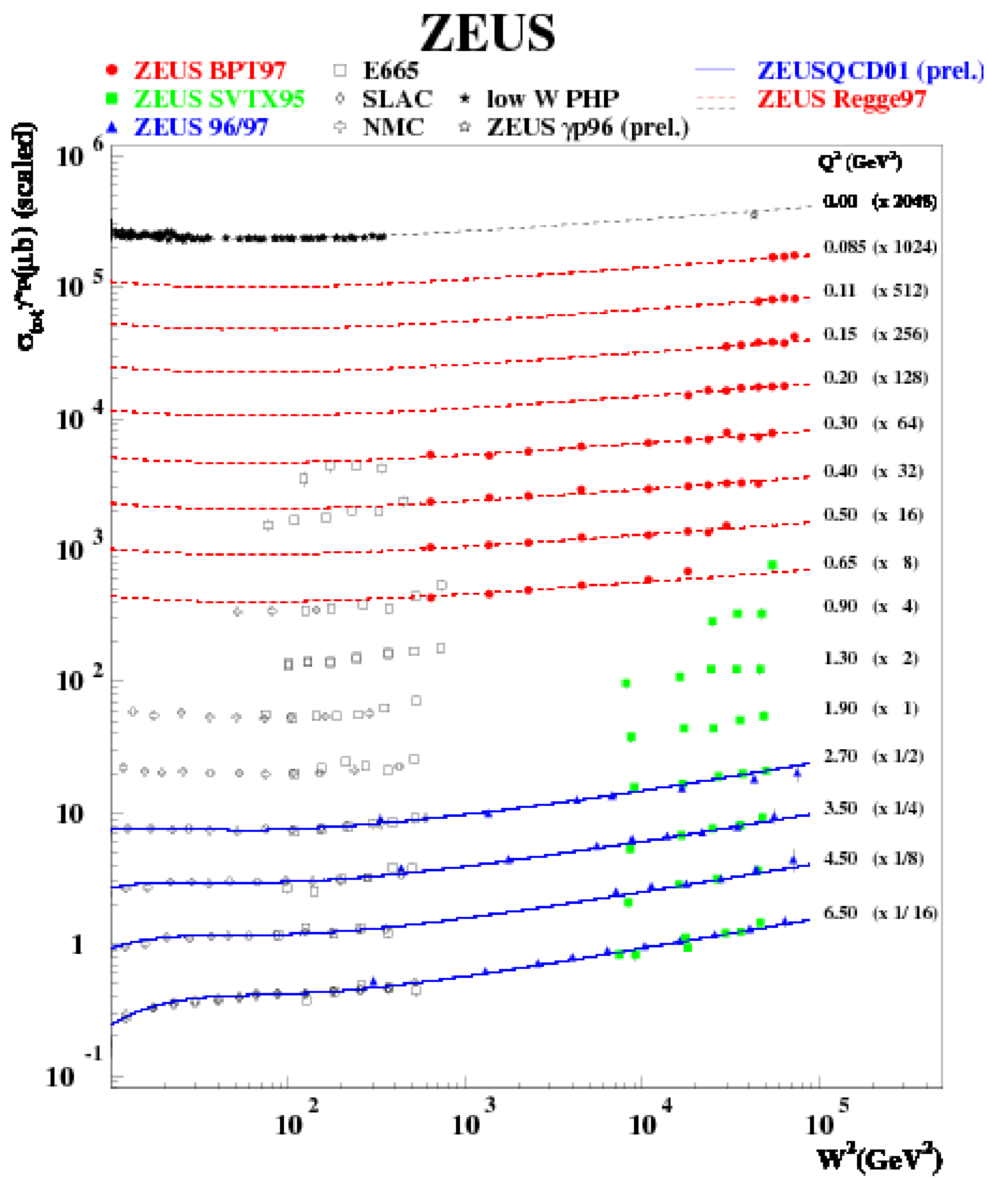

Figure 2.4: The total cross-section of photon-hadron scattering, σ_{tot}, as a function of different W^2 and Q^2.

2.4 Photon-proton collisions

A combination of VDM and Regge phenomenology can be applied to describe the diffractive physics processes at HERA. Photon-proton interaction at HERA can be categorized in four processes;

- Elastic scattering $(\gamma^* p \to Vp)$ - the photon fluctuates into a vector meson, which scatters quasi-elastically off the proton
- Photon dissociation $(\gamma^* p \to Xp)$ - the photon fluctuates into a vector meson, which dissociates into a higher mass state, X, while the proton stay intact
- Proton dissociation $(\gamma^* p \to VY)$ - the photon fluctuates into a vector meson, which remain intact, while the proton dissociates into a higher mass state, Y
- Double dissociation $(\gamma^* p \to XY)$ - the photon fluctuates into a vector meson, which dissociates into a higer mass state, X, and the proton dissociates into a higher mass state, Y.

A typical signature of diffractive events at high energies is a large rapidity gap. The schematic presentation of energy flow for non-diffractive and diffractive events is shown in Figure 2.5 below.

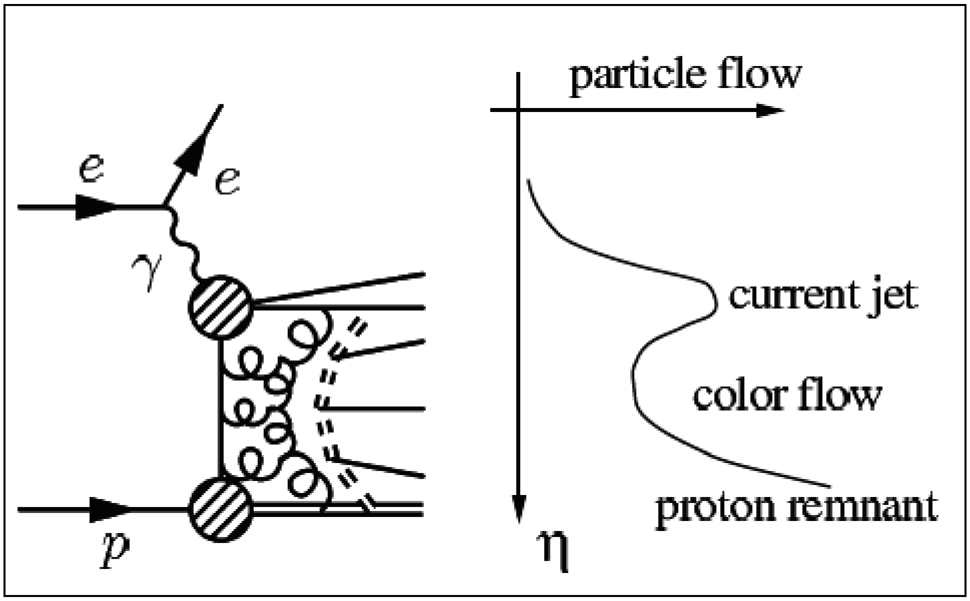

(a) non-diffractive event

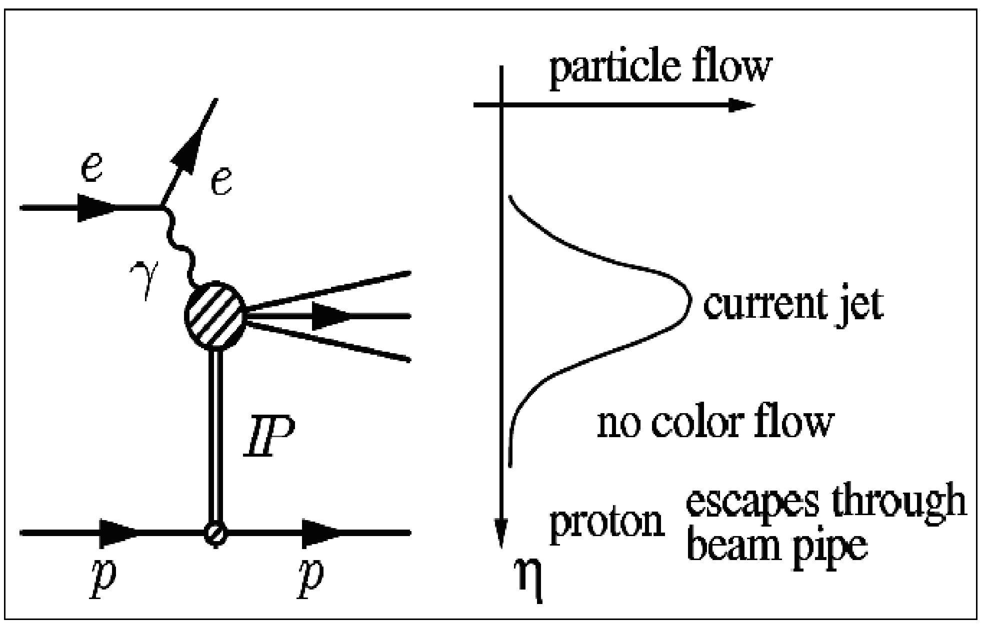

(b) diffractive event

Figure 2.5: The schematic presentation of energy flow in non-diffractive and diffractive event with large rapidity gap at HERA.

2.5 Relation between *ep* and $\gamma^{*}p$ scattering

In the one photon exchange (Born) approximation the electron-proton scattering may be regarded as a scattering of the virtual photon off the proton. The inclusive double differential *ep* cross section may be described in terms of two absorption cross sections, $\sigma_T^{\gamma^* p}$ and $\sigma_L^{\gamma^* p}$, corresponding to the transverse and longitudinal polarisations of the virtual photon:

$$\frac{d^2\sigma^{ep}}{dQ^2 dy} = \Gamma_T \sigma_T^{\gamma^* p} + \Gamma_L \sigma_L^{\gamma^* p} = \Gamma_T (\sigma_T^{\gamma^* p} + \in \sigma_L^{\gamma^* p}), \tag{9}$$

where Γ_L and Γ_L are the longitudinal and transverse photon fluxes [12]:

$$\begin{aligned} \Gamma_L(y,Q^2) &= \frac{\alpha}{2\pi Q^2}\frac{2(1-y)}{y}, \\ \Gamma_T(y,Q^2) &= \frac{\alpha}{2\pi Q^2}\left(\frac{1+(1-y)^2}{y} - \frac{2(1-y)}{y}\frac{Q^2_{\min}}{Q^2}\right) \end{aligned} \tag{10}$$

Where

$$Q^2_{\min} = m_e^2 \frac{y^2}{1-y} \tag{11}$$

is the minimum of Q^2 kinematically allowed and $\in$ is the ratio of the fluxes

($0 < \in < 1$):

$$\in = \frac{\Gamma_L}{\Gamma_T} = \frac{2(1-y)}{1+(1-y)^2} \tag{12}$$

The total $\gamma^{*}p$ cross section:

$$\sigma^{\gamma^{*}p} = \sigma_{T}^{\gamma^{*}p} + \sigma_{L}^{\gamma^{*}p} \tag{13}$$

is related to the inclusive *ep* cross section as follows:

$$\frac{d^{2}\sigma^{ep}}{dQ^{2}dy} = \Gamma_{T}\left(\frac{1+\in R}{1+R}\right)\sigma^{\gamma^{*}p}(y,Q^{2}) \tag{14}$$

where R is the ratio of cross sections for the longitudinally and transversely polarised virtual photons:

$$R = \frac{\sigma_{L}^{\gamma^{*}p}}{\sigma_{T}^{\gamma^{*}p}} \tag{15}$$

The proton structure functions are related to $\gamma^{*}p$ cross sections by the following relations:

$$\begin{aligned} F_{2}(x,Q^{2}) &= \frac{Q^{2}}{4\pi^{2}\alpha}\sigma^{\gamma^{*}p}(x,Q^{2}), \\ F_{L}(x,Q^{2}) &= \frac{Q^{2}}{4\pi^{2}\alpha}\sigma_{L}{}^{\gamma^{*}p}(x,Q^{2}) \end{aligned} \tag{16}$$

2.6 Exclusive Vector Meson Photoproduction

Photoproduction (PHP) process mainly describe the interaction of photon to proton after the *ep* collision at low energy of Q^2 <1 GeV. At this energy level, the scattered electron, *e'* shall remain undetected in the beampipe of the detector as well as the scattered proton or hadrons. These features are the main signature of PHP events. The illustrated picture of this interaction can be seen in the schematic diagram shown in Figure 2.5. Meanwhile, the word 'exclusive' refers to the elastic scattering which means, the interaction between photon and proton does not yield any inclusive processes inside the proton and the photon will fluctuate into a vector meson (VM), which scatters elastically off the proton. This terminology also due to the underlying two-body scattering process $\gamma^* p \quad Vp$, in which the proton stays intact and the VM holds the quantum number of the incident γ^*. The process area only primarily concurred at the photon-proton vertex which holds a precise number of particle produced. More specific explanations will be given in Chapter 5.

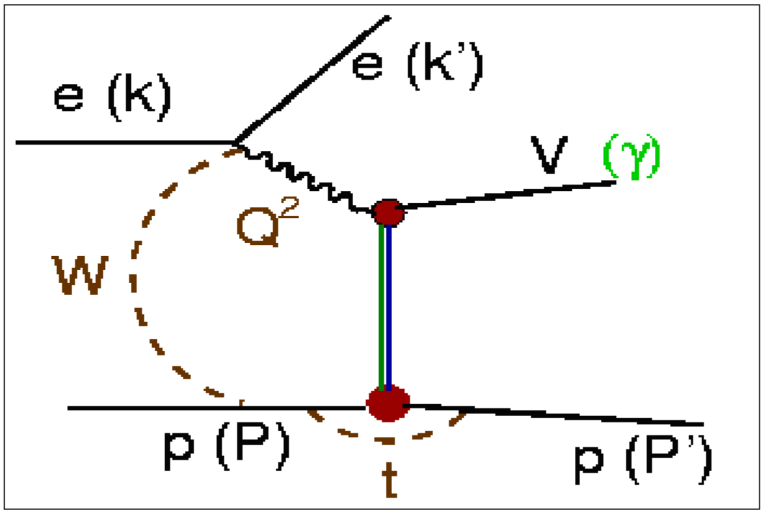

Figure 2.6: Schematic diagram of VM production.

2.7 Acceptance and γp Cross Section

The acceptance (A) and particle cross-section (σ) are the variables used to determine the production rates of the particular search particle and the likelihood of interaction between particles. Calculations and results of this analysis are shown in chapter 5 of this thesis.

2.7.1 Acceptance Calculation on Monte Carlo (MC)

The acceptance or production rate of a particle can be determined based on the ratio of the particle entries in the signal compared to the particle generated number using MC. The number of reconstructed particle N_p, is determined by calculating the particle entries of the signal which usually done by graph fitting procedure. The fitting algorithm will be describe later in analysis part of this thesis.

Acceptance (A) can be obtained from the following relation;

$$A = \frac{N_P}{N_G} \tag{17}$$

Where N_P is the number of particle produced in the signal and N_G is the number of particle generated in events.

2.7.2 γp Cross-Section Calculation

The γp cross-section defines as the ratio of *ep* cross-section over the effective photon flux in the specific value of W and Q^2 measured in the range of W(min:max) and Q^2(min:max).

The calculation can be done using the formula:

$$\sigma(Q^2, W) = \frac{\sigma_{ep}}{\Phi} \tag{18}$$

Where Φ is the effective photon flux and σ_{ep} is the cross section for *ep* interaction.

The σ_{ep} can be obtained by,

$$\sigma^{ep \rightarrow \psi(2S)p} = \frac{N_{\psi(2S)}}{ABL} \tag{19}$$

Where *A* is the acceptance, *B* indicates the branching ratio of the decay channel and *L* is the luminosity measured in the experiment.

$$\sigma^{\gamma p \to \psi(2S) p} = \frac{\sigma^{ep \to \psi(2S) p}}{\Phi} \tag{20}$$

And the effective photon flux, Φ can be calculated using following formula [12];

$$\Phi_{eff}^{\gamma p \to \psi(2S) p} = \int \Phi(y, Q^2) dy dQ^2 \tag{21}$$

$$\Phi(y, Q^2) = \frac{\alpha}{2\pi Q^2}\left[\frac{1+(1-y)^2}{y} - \frac{2(1-y)}{y}\left(\frac{Q^2_{\min}}{Q^2} - \frac{Q^2}{M^2_{\psi(2S)}}\right)\right]\left(1+\frac{Q^2}{M^2_{\psi(2S)}}\right)^{-2} \tag{22}$$

Where, $y = \frac{W^2}{s}$ and $Q^2_{\min} = M^2_{el}\frac{y^2}{(1-y)}$.

These equations will be implemented in the analysis part of this thesis and the results are shown in chapter 5.

CHAPTER 3

EXPERIMENTAL SETUP

3.1 ZEUS Experiment

ZEUS experiment began its first operation in 1992. The experiment mainly consists of two main giant equipments, the HERA collider and ZEUS detector, which used to accelerate and detect particle from electron and proton collision respectively. Generally, the experiment is dedicated to observe the particles productions at high energy physics events of lepton-hadron collision as well as observing the particle characters.

3.2 HERA Collider

The HERA ring is located at DESY, Hamburg. It was constructed 30m underground deep and 6.3km long in circumference. It was the first e-p collider designed to accelerate the electron and proton from opposite direction before collisions take place inside the detection system or detector.

The electron and proton beampipe are placed on top of each other along the HERA ring. The electron beampipe consist of normal conducting dipole-magnets with 0.3T and super-conducting cavities to accelerate electron beam up to 27.5 GeV. Meanwhile the proton beampipe has the feature of 4.7 T dipole-magnets conductivity and can be accelerated up to 920 GeV in HERA ring. The squared centre-of-mass energy for e-p collision, $\sqrt{s}$ was measured to be 300 until year 1997 and then changed to 318 after the e-p acceleration energy upgrading until the operation stopped in 2007. HERA was built with four interaction points where detectors are placed. The H1 and ZEUS detectors are designed for the e-p interaction. Meanwhile HERMES is used for research on the spin structure which only utilizes an electron beam. The forth detector, HERA-B investigates CP violation in the $B^0\overline{B}^0$-system by using the proton beam together with a fixed wire target. Each of these experiments have contributed significantly to for particle physics research.

The proton and electron originate at different starting points. Protons were firstly stripped off from negative hydrogen ions (H^-) in LINAC III and injected with energies of 50 MeV. Then the proton was transferred to the DESY III ring and injected to 7 GeV before moving to the bigger ring of PETRA with a higher energy injection of 40 GeV. Lastly, the proton was transferred to the biggest ring, HERA with the highest energy of 920 GeV. Meanwhile, electrons started at LINAC II with energies of 450 MeV before moving to DESY II ring with higher energy injection of 7.5 GeV. Moving on to PETRA, the energy of the electrons were subsequently injected up to 14 GeV and ready to accelerate at highest energies of 27.5 GeV in HERA afterwards. HERA could be filled with a maximum of 210 bunches of leptons and protons at a time where each of them were separated by 96 ns [13-16].

Figure 3.1: An aerial view of HERA showing the location of the accelerators.

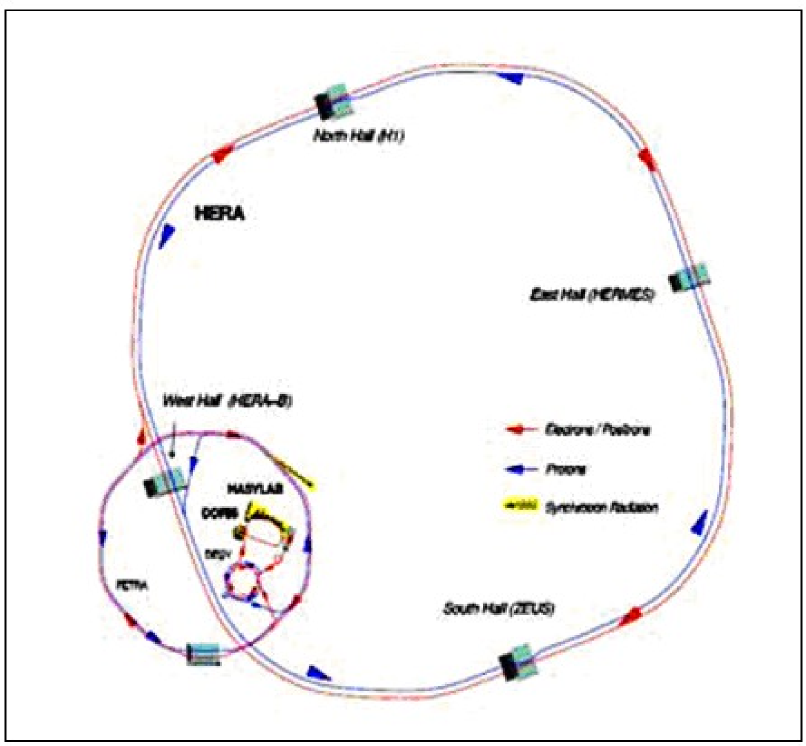

Figure 3.2: This diagram shows the direction of the electron and proton injection flows. The red arrow represents the electron and the blue arrows represent the proton.

3.3 ZEUS Detector

The ZEUS detector [17] was located 30 m underground at south direction of HERA. The weight was about 3500 tons and was 12 meters in height. It was a multipurpose detector with a solid angle coverage of 99.6% and implement the right-handed schematic system. The centre of the system was at the nominal interaction point (IP), the z-axis was pointing to the forward direction (proton direction), the x-axis was pointing towards the centre of HERA and the y-axis was pointing upward.

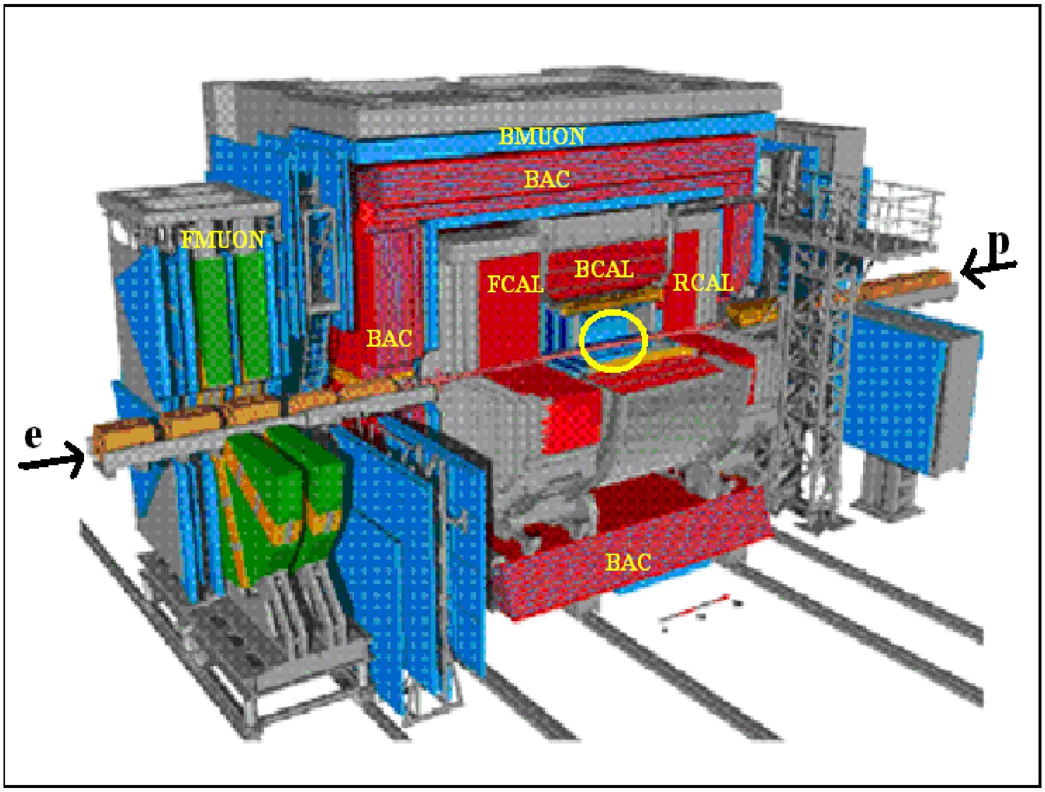

Figure 3.3: The picture shows a 3-dimentional view of a ZEUS detector, its main components and the electron proton directions. The circled area indicates the interaction point of the electron proton collision.

The polar angle, θ and the azimuthal angle, ϕ were measured relative to the z and x axes respectively. Usually, θ angle was described in pseudorapidity form, $\eta = -\ln\left(\tan\frac{\theta}{2}\right)$. There was an obvious symmetry imbalance between the forward and rear side of the detector. The forward side was longer than the rear part. This was because of the huge different in momentum values of proton and electron, which giving a bigger particle boosting towards the forward direction.

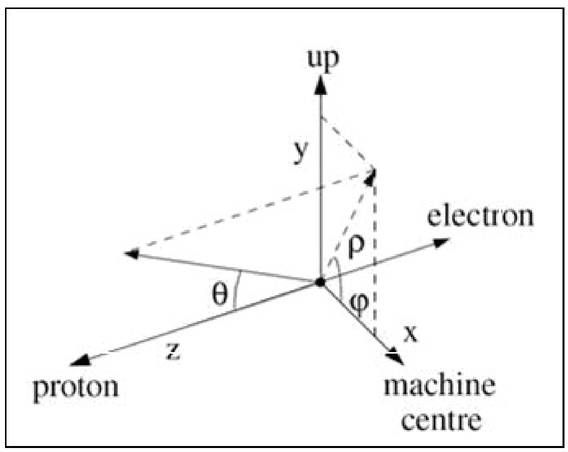

Figure 3.4: The picture shows the coordinate system of the ZEUS detector.

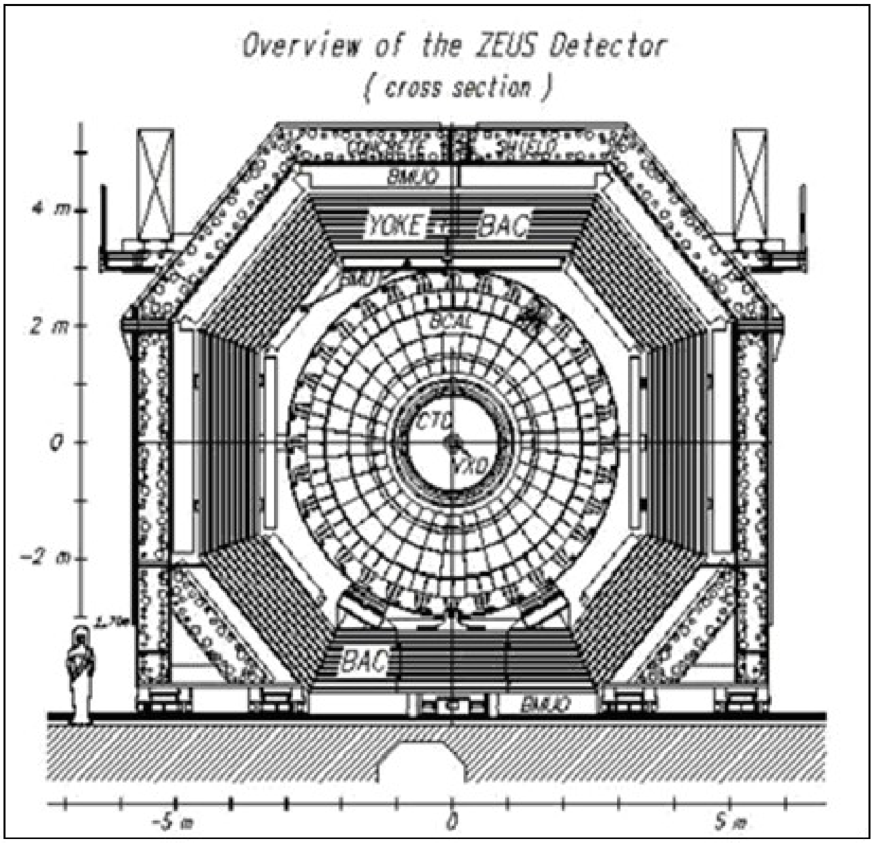

Figure 3.5 : Cross section of the ZEUS detector in x-y plane.

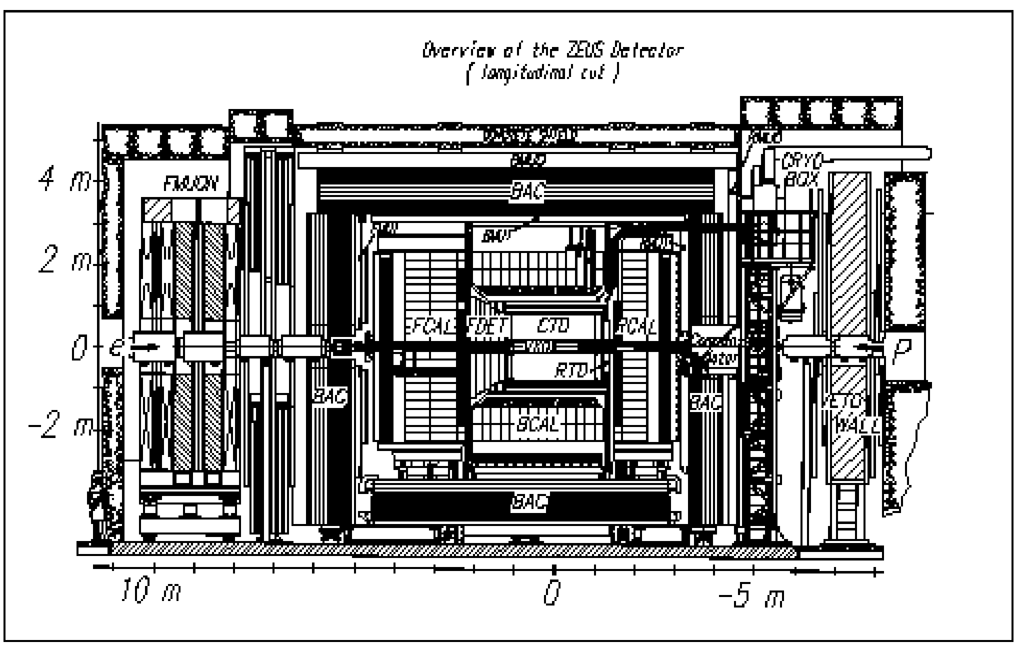

Figure 3.6: Cross section of the ZEUS detector in z-y plane.

3.4 Muon Detection System

The muon is recognized as a minimum ionizing particle (MIP) which leaves tracks signature in many different subdetectors such as tracking, calorimeter and the external muon detection systems. It has a high penetration power allowing it to go through almost all detector layers. The range of muons in iron is about 1 m/GeV. Basically in ZEUS detector, there are three main components of muon detectors; the forward muon detector (FMUON), the barrel muon detector (BMUON) and the real muon detector (RMUON). Figure 3.7 and 3.8 shows the picture of the muon detector components in ZEUS detector.

The muon finder for the ZEUS detector is called the GMUON. It is a combination of all muon finders available at ZEUS. It establishes links between finders and assigns a global muon quality. The GMUON is implemented in the context of ORANGE analysis environment. The cross reference to the other ORANGE information (tracks, jets, MC true and etc.) also provided. Traditionally, we need a specific selection of one or two such algorithm which was available as private code in each muon analysis. Obviously, this process is a tedious way of doing the analysis. To have more efficiency in muon analysis, the GMUON [43] finder has been created. The purpose of GMUON is to combine the most important information from different finders into a common format without private code. It is also able to combine information of the same muon from different finders into single entries as much as possible. Users also have freedom to select their finders and cuts as the GMUON will provide cross reference to the individual finders. GMUON also provide a global muon quality flag which allow the average user to preselect muons without need to know all the details about finders.

Muon can be detected in different ways and signature. It can be identified by the characteristic of its charge penetration in the subdetector. The tracks of this penetration can be seen in the inner tracking detector such as the Micro Vertex Detector (MVD), Central Tracking Detector (CTD) [18-20], and so on. These tracks are bent in the ZEUS solenoid field and their curvature can be used to determine the muon momentum. The muons that are famous in physics are produced either directly at the primary vertex, or in semileptonic heavy flavor decays very close to the primary vertex. Muons, as a MIP particle, lose a well defined amount of energy in the calorimeter along their trajectory. This energy loss is almost independent of muon momentum. The pattern of this energy loss is significantly important to identify muons which do not overlap with any other particles and well isolated. Since the other particles will lose all their energy in the calorimeters, therefore the separation power for muon detection using the MIPs increases with the increasing muon momentum. However, if the muon is a non-isolated particle which overlaps with other particles, MIPs cannot be used in the detection.

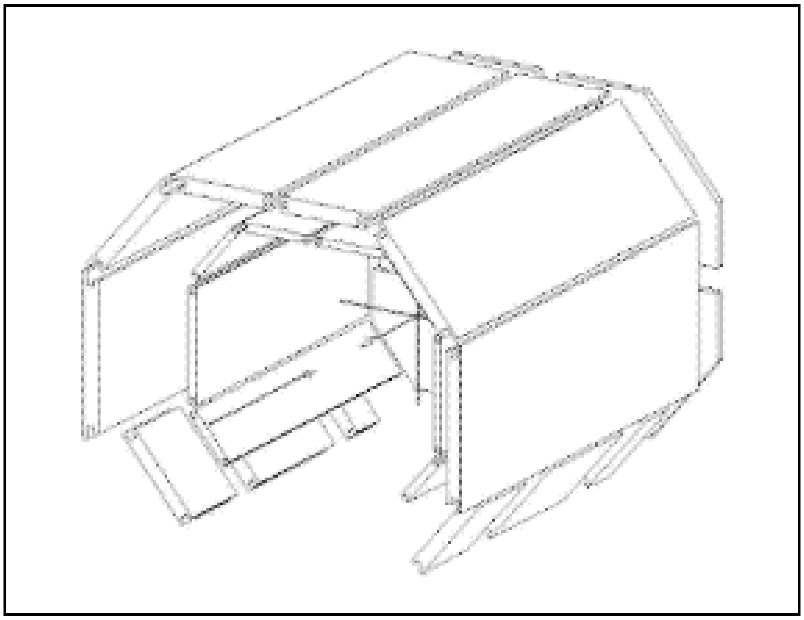

Figure 3.7 : 3D structure of BRMUON

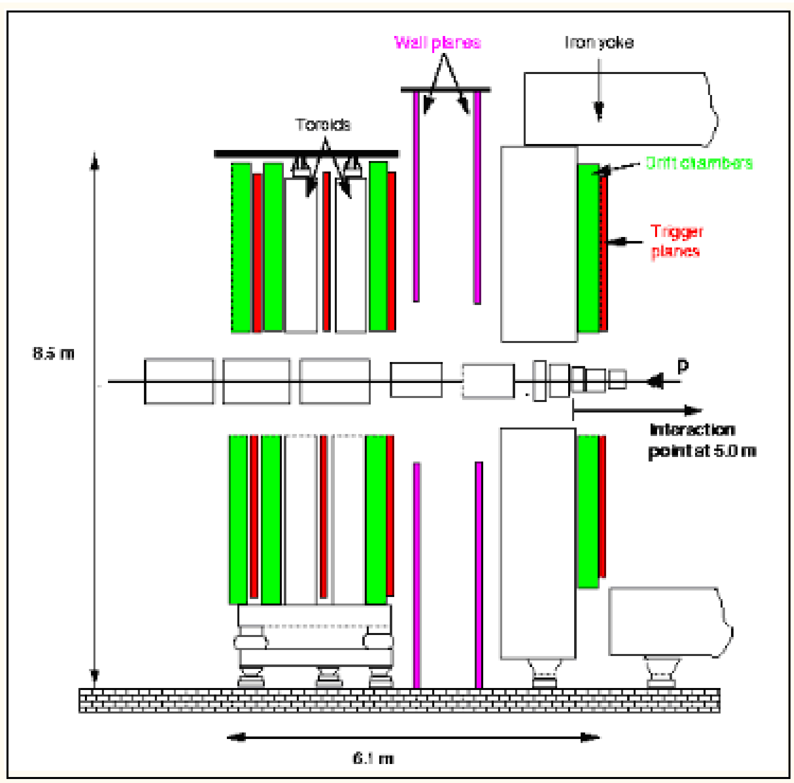

Figure 3.8 : Cross section of FMUON

3.5 Central Tracking Detector (CTD)

The CTD [18-20] is a cylindrical wire drift chamber with a magnetic field of 1.43 T which is provided by a thin superconducting solenoid. The CTD is used to measure the directions and momenta of the charged particle and estimate the energy loss dE/dx to provide information for particle identification. It has 72 cylindrical drift chamber layers of sense wires, organized in 9 superlayers covering the polar angle 15° to 164°. Each superlayer consist of 8 sense wires with associated field wires, called a cell. The drift cells of all superlayers are similar. There are a total of 4608 sense wires and 19584 field wires in the CTD. The inner radius of the chamber is 79.4cm, and its active region covered the longitudinal distance of -100 cm $< z <$ 104 cm. The sense wires were 30 μm thick while the field wires have different diameters. Each superlayer was numbered accordingly from the inner layer to the outer layer. The odd layer consists of tools which were used to determine the z-position by using the time different between the arrival times of the signal from the opposite end of the CTD. The CTD was filled with a mixture of argon (Ar), carbon dioxide (CO_2) and ethane (C_2H_6) in the ratio 85 : 5 : 1. A charged particle crossing the CTD produced ionization of the gas in the chamber. The electrons from the ionization drifted towards the positive sense wires whereas the positively charged ions drifted toward the negative field wires. The CTD hit resolution of HERA I was 200 μm in the $r-\phi$ plane and 2 mm in the z coordinate. The resolution on p_T for tracks fitted to the interaction vertex and passing at least three CTD superlayers and with p_T > 150 MeV, is given by:

$$\frac{\sigma(p_T)}{p_T} = 0.0058 \cdot p_T \oplus 0.0065 \oplus \frac{0.0014}{p_T}$$

where p_T is given in GeV and the symbol $\oplus$ indicates the quadratic sum. Meanwhile for HERA II, the new additional tracking equipment has been installed to improve the tracking resolution which is called the micro vertex detector (MVD).

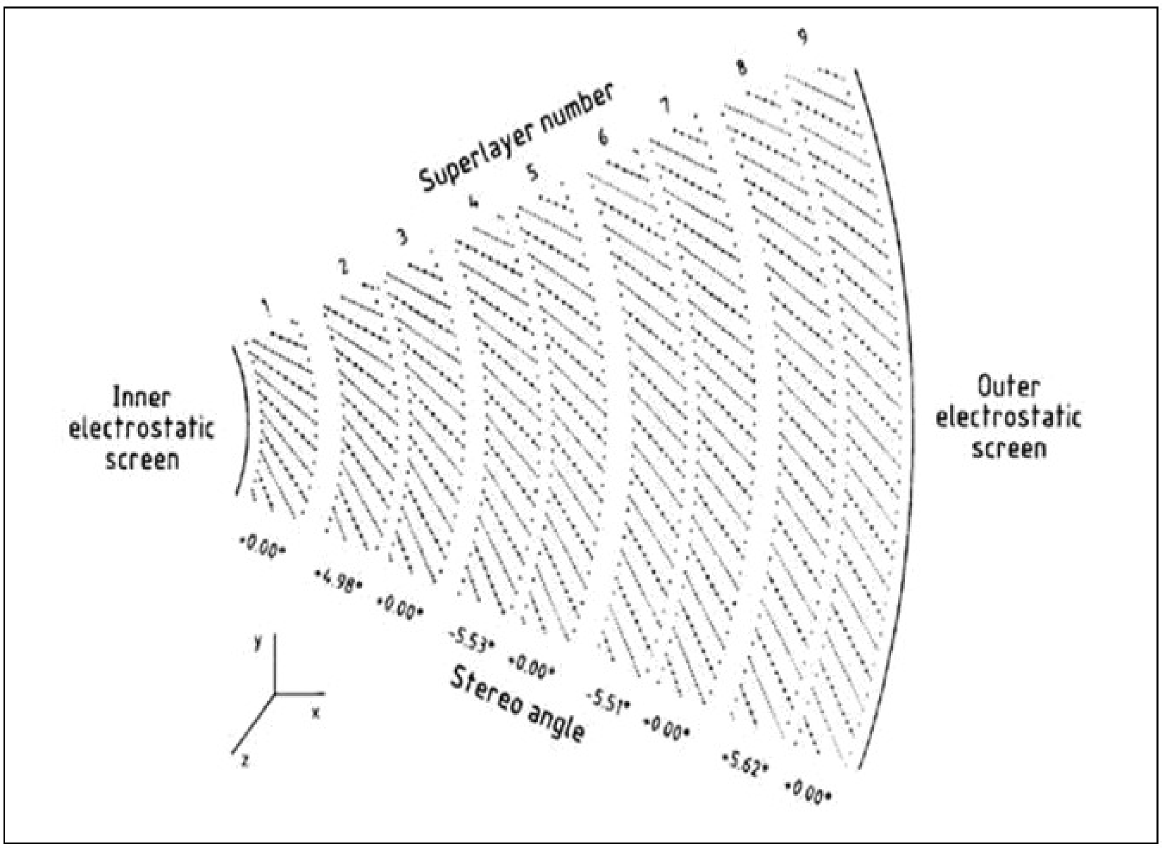

Figure 3.9: Layout of a CTD octant. The superlayers are numbered and the stereo angles of their sense wires are shown.

3.6 Micro Vertex Detector (MVD)

The silicon-strip micro vertex detector (MVD) [21] was installed in 2001. It aimed at a significant improvement of the tracking capabilities to permit the reconstruction of impact parameters and secondary vertices. Figure 3.10 displays the layout of the MVD, which is split into a barrel and a forward region. The sensitive areas are called ladders and contain two layers of orthogonally oriented silicon strips.

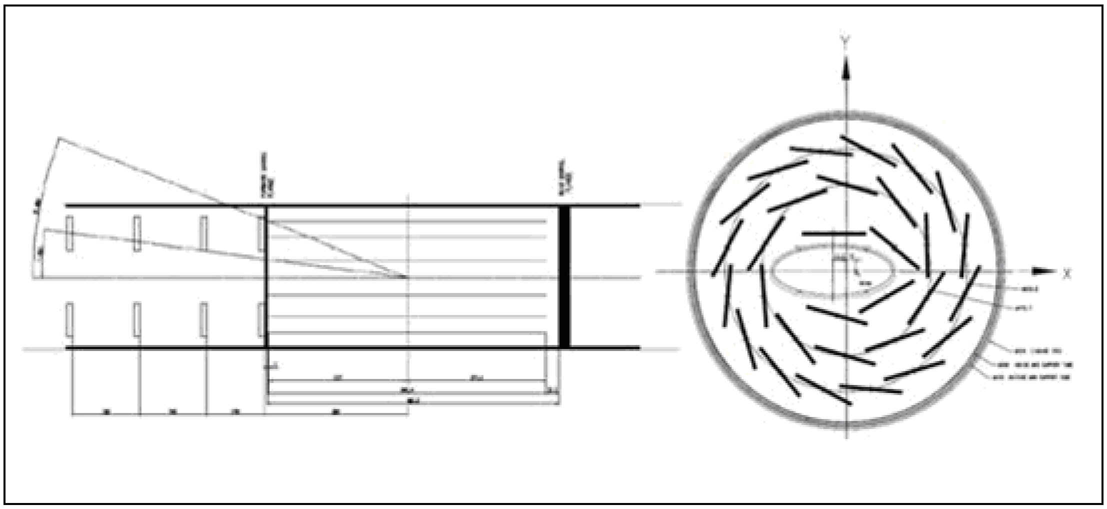

Figure 3.10: Cross sections of the MVD along the beam pipe (left) and in the X-Y plane (right).

The MVD measured the charge-deposit on its strips. In combination with the known geometry of the detector and the orientation of the tracks this was used to measure the ionization rate. It is possible to use the MVD for particle identification in a similar way as the CTD. As one can observe in Fig. 3.10 a typical track passes 3 ladders, i.e. at most 6 silicon strips. This number is small compared to the number of hits for a typical track in the CTD. Performance comparison of the tracking used for HERA I data samples (CTDonly) to the tracking used for the HERA II data (MVD-CTD: 2003-2007, and MVD-CTD-STT: 2003-2007 excluding 2005) is not a trivial task.. The track transverse momentum resolution improved by ≈ 50%. The vertex position in x-y plane improved changing from ~ 0.1 cm (HERA I) to better than 0.01 cm (HERA II). The z-coordinate of the vertex position also improved due to a few extra hits located closer to the interaction point, however having no consequences for the analysis. The cuts defining the vertex position in x, y, z coordinates were conservative remaining identical to the ones used in the analyses of HERA I data samples only.

3.7 Forward and Rear Tracking Detectors (FTD, RTD)

The FTD [22] measured the tracks of charged particles in planar drift chambers located at the ends of the central tracking detector in forward (proton) and rear (electron) directions.

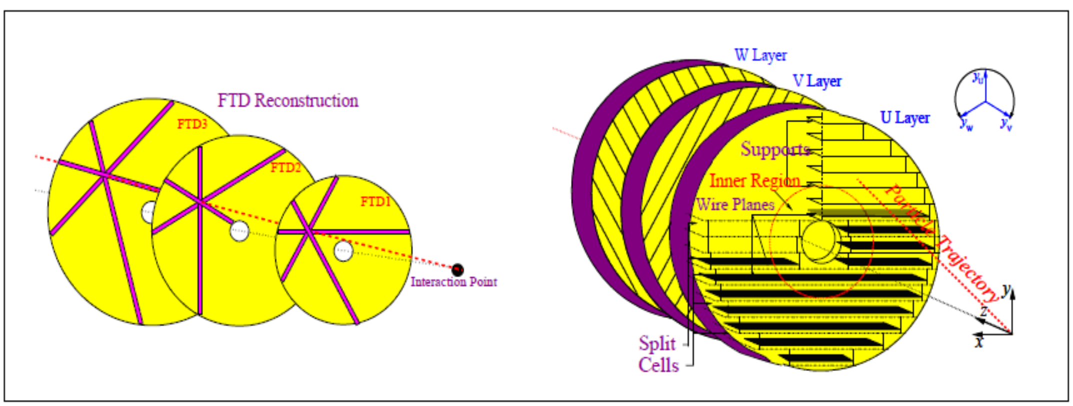

Figure 3.11: The Layout of the FTD drift chambers in (left) overall view and (right) view of the 3 layers inside of one of the chambers.

A charged particle passed in the FTD through 3 chambers (RTD - 1 chamber). Each chamber contained 3 layers with a total of 18 wire planes. The layers consisted of drift cells which were rotated by 60 degrees with respect to each other. The FTD cells are rectangular with six signal wires strung perpendicular to the beam axis.

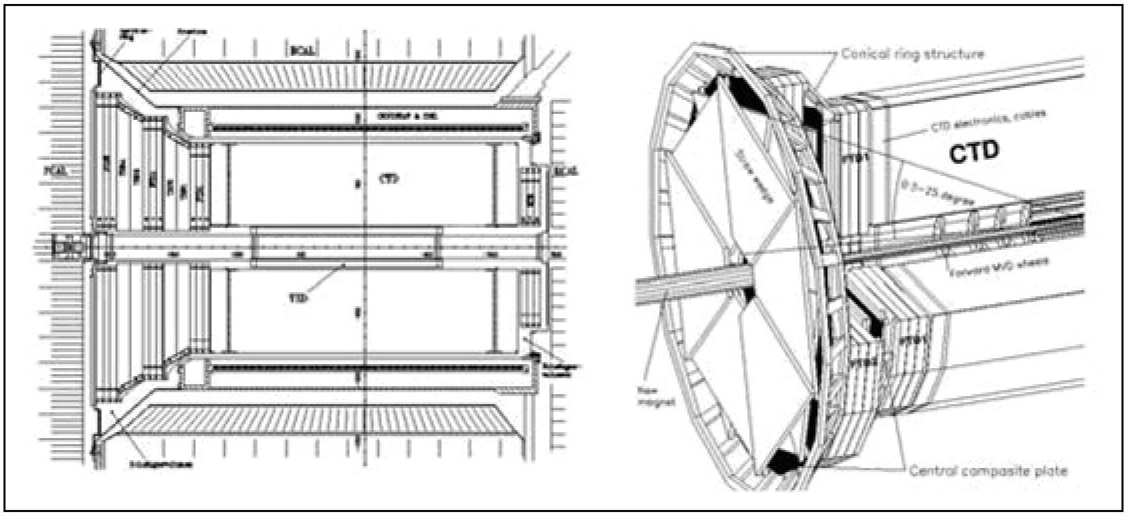

Figure 3.12: (left) a view of the tracking detectors, in the forward area the four tracking detectors planes are shown, which were replaced with two straw-tube tracker (STT) [23] wheels, (right) the angular coverage of the STT compared to the CTD and forward MVD wheels.

3.8 Uranium Calorimeter (CAL)

The ZEUS calorimeter (CAL) [24-27] is a high-resolution compensating calorimeter. It completely surrounds the tracking devices and the solenoid, and covers 99.7% of the 4π solid angle. It consists of 3.3 mm thick depleted uranium plates (98.1% U^{238}, 1.7% Nb, 0.2% U^{235}) as absorber alternated with 2.6 mm thick organic scintillators (SCSN-38 polystyrene) as active material. The thickness of the absorber and of the active material have been chosen in order to have the same response for an electron or a hadron of the same energy passing through the detector (*e/h* = 1.00±0.05). This mechanism is called compensation, and allows achieving good resolution in the determination of both the electromagnetic and the hadronic energy.

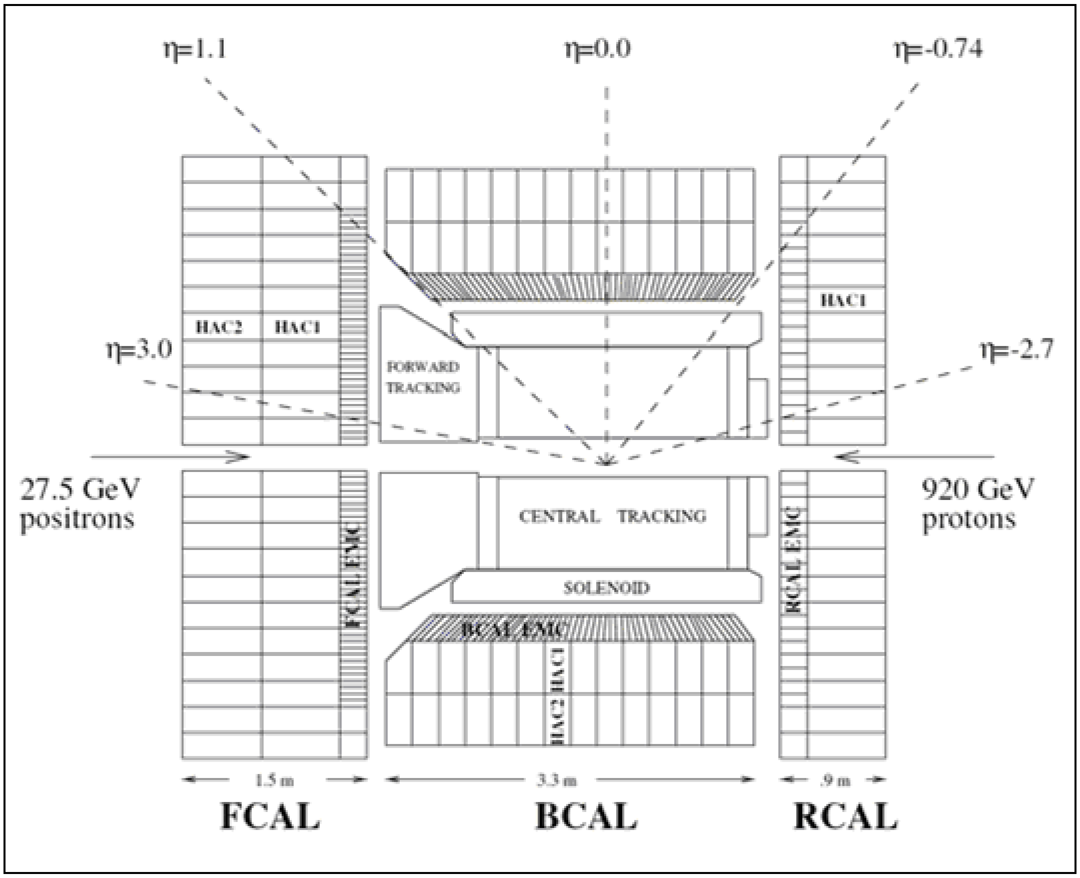

Figure 3.13: Cross section of the ZEUS CAL in the y-z plane.

The achieved hadronic energy resolution is

$$\frac{\Delta E}{E} = \frac{35\%}{\sqrt{E}} \oplus 1\% \qquad (23)$$

while the electromagnetic resolution is

$$\frac{\Delta E}{E} = \frac{18\%}{\sqrt{E}} \oplus 2\% \tag{24}$$

where ΔE is the particle energy, measured in GeV. The CAL is divided into three parts: the forward (FCAL), barrel (BCAL) and rear (RCAL) calorimeters.

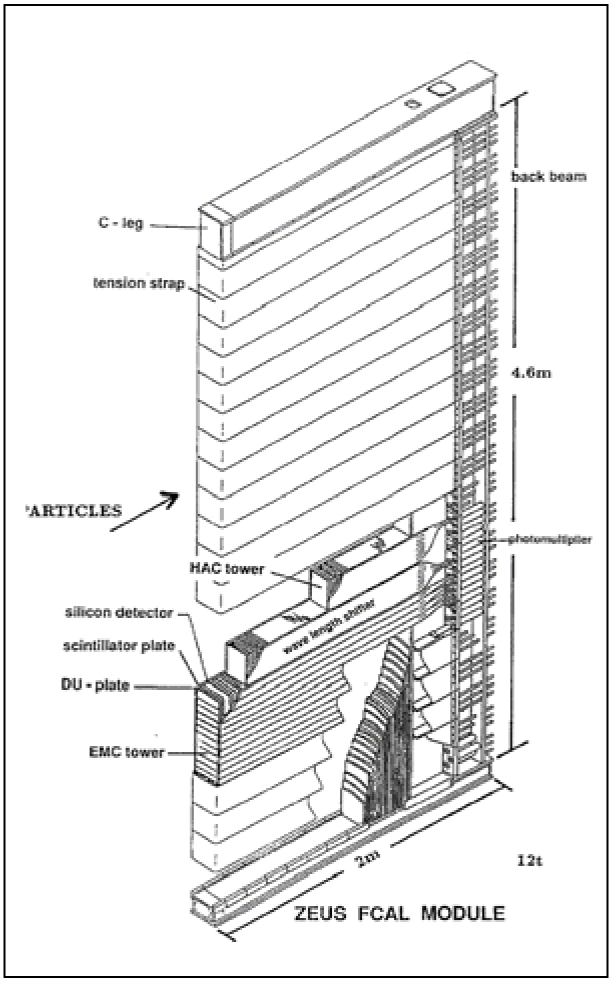

Figure 3.14: View of an FCAL module. The towers containing the EMC and HAC sections are shown.

The three parts are of different thickness, the thickest one being the FCAL (~ 7λ), then the BCAL (~ 5λ) and finally the RCAL (~ 4λ), where λ is the track length. Each part of the calorimeter is divided into modules, and each module is divided into one electromagnetic (EMC) and two (one in RCAL) hadronic (HAC) sections. These sections are made up of cells, whose sizes depend on the type (EMC or HAC) and position (in FCAL, BCAL or RCAL) of the cell. The FCAL consists of one EMC (first 25 uranium-scintillator layers) and two HAC (remaining 160 uranium-scintillator layers) sections. The electromagnetic section has a depth of ≈ 26 X_0, while each hadronic section is 3.1 λ deep.

The EMC and HAC cells are superimposed to form a rectangular module, one of which is shown in Fig. 3.14 and 23 of these modules make up the FCAL. The BCAL consists of one EMC and two HAC sections, the EMC being made of the first 21 uranium-scintillator layers, the two HACs of the remaining 98 layers. The resulting depth is 21 X_0 for the electromagnetic section, and 2 λ for each hadronic section. The cells are organised in 32 wedge-shaped modules, each covering 11.25^o in azimuth. The RCAL is made up of 23 modules similar to those in the FCAL, but it consists of one EMC and only one HAC section. Therefore its depth is 26 X_0 for the EMC part and 3.1 λ for the HAC part. The light produced in the scintillators is read by 2 mm thick wavelength shifter (WLS) bars at both sides of the module, and brought to one of the 11386 photomultiplier tubes (PMT) where it is converted into an electrical signal. This information is used for energy and time measurements. The CAL provides accurate timing information, with a resolution of the order of 1 ns for tracks with an energy deposit greater than 1 GeV. This information can be used to determine the timing of the particle with respect to the bunch-crossing time, and it is very useful for trigger purposes in order to reject background events. The stability of the PMTs and of the electronics is monitored with lasers and charge pulses. In addition, the small signal coming from the natural radioactivity of the depleted uranium gives a very stable signal, also used for the calibration. The achieved accuracy is better than 1%.

3.9 Monte Carlo Generator for Vector Meson

The simulation of the vector meson production and decay is implemented in the DIFFVM 2.0 [28] software package. The software program implements Regge phenomenology and the Vector Dominance Model (see Chapter 2.3.2) with a set of parameters, which can be set via control cards. S-Channel Helicity Conservation (SCHC) is assumed in the generation of the angular distribution of the decay products. The program is primarily used to generate samples of elastic production of the vector mesons. Processes with dissociation of the proton can be generated as well. For the generation of the proton remnant spectrum DIFFVM uses a parametrisation of the experimental data of the mass spectra of excited states of hadrons. This spectrum consists of some resonances-like structures superimposed on the diffraction dissociation continuum. The inclusive cross section for diffractive processes, at fixed t, can be parametrised as follows:

$$\frac{d\sigma}{dM_Y^2} \sim \frac{f(M_Y^2)}{M_Y^{2(1+\epsilon)}} \tag{25}$$

where $f(M_Y^2)$ is a function of the diffractive mass at the proton vertex accounting for the low mass behaviour, including the resonance states.

DIFFVM uses the following parametrisation for this function:

- in the continuum region ($M_Y^2 \geq 3.6$ GeV^2), $f(M_Y^2) = 1$; this reproduces the behaviour $\sim \frac{1}{M_Y^{2(1+\epsilon)}}$ of diffractive dissociation,
- in the “resonance region” ($M_Y^2 < 3.6$ GeV 2), $f(M_Y^2)$ is the result of a fit of the measured differential cross section, at fixed t, for proton diffractive dissociation on deuterium $pD \to YD$;

The continuum state may dissociate into a quark-diquark system (simulated via JETSET) or decay isotropically. The t-distribution b parameter is set:

$$b(W, M_Y) = b(W_0, M_0) + 4\alpha'_p \left(\ln\frac{W}{W_0} - \ln\frac{M_Y}{M_0} \right) \tag{26}$$

and is assumed to hold at all values of $Q2$.

The W and $Q2$ dependence of the cross section is given by:

$$\sigma^{\gamma^* p}(Q^2, W) \sim \frac{W^\delta}{(Q^2 + M_V^2)^n} \tag{27}$$

where n ≈ 2.5 is an empirical parameter, $\delta = 4(\alpha\, p\, (0) - 1)$ and M_V mass of the vector meson.

The ratio of the cross sections of the photons with transverse and longitudinal polarisation is given by:

$$R(Q^2) = \frac{\xi \frac{Q^2}{\Lambda^2}}{1 + \chi\xi \frac{Q^2}{\Lambda^2}} \tag{28}$$

where Λ, χ, ξ are free parameters. The recommended values are $\Lambda = M_V$, $\chi = 0.66$, $\xi = 0.33$.

CHAPTER 4

TRACKING EFFICIENCY

4.1 Tracking concepts in detector

Tracking layout of a detector typically reflects the whole view and physics purpose of the experiment. Every single part or components are constructed within the physics event required and this will mention the structure of the tracking chambers, which is known as one of the most important part of detector. In common scenarios, there are two typical concepts of tracking structure in detector, the forward or fixed-target geometry and the collider detector geometry.

4.1.1 Forward or fixed-target geometry and parameters

In the fixed-target geometry concept, the colliding or incident particle is assumed to have significantly high momentum with a huge effect of Lorentz boost. After hitting the static target in the middle of detector, emerging particles will travel forward in a cone-shaped region. To cover all possible trajectory space, in this situation, the detector layout must essentially manage to cover every single angle of the projected cone. Meanwhile, in most practice, the backward part of the solid angle is neglected and this gives the reason why this scenario is called the forward detector geometry concept.

Below are the main components of the typical forward spectrometer:

- The vertex detector, whose main purpose is to improve track detection with higher resolution near the interaction point. Reconstruction of secondary vertex or distinction of detached tracks is an important aspect of particle reconstruction in the detector.
- The spectrometer magnet and the main tracking system in forward geometry which measures momentum and determine the sign of charged particles from the curvature.
- The calorimeter system, measures the deposited shower energy from particle trajectories which then allows the identification of electrons and hadrons. The component is split into two parts, electromagnetic and hadronic. The calorimeter also measure energies of individual neutral particles, usually photons.
- The muon detector, placed at the last part of spectrometer. Muons typically having longer lifetime, are able to traverse the intermediate materials and will be detected at specific dedicated tracking layers.

The design of forward spectrometer is also influenced by the momentum resolution as at sufficiently high momentum the resolution is inversely proportional to the integral of the magnetic field along the trajectories.

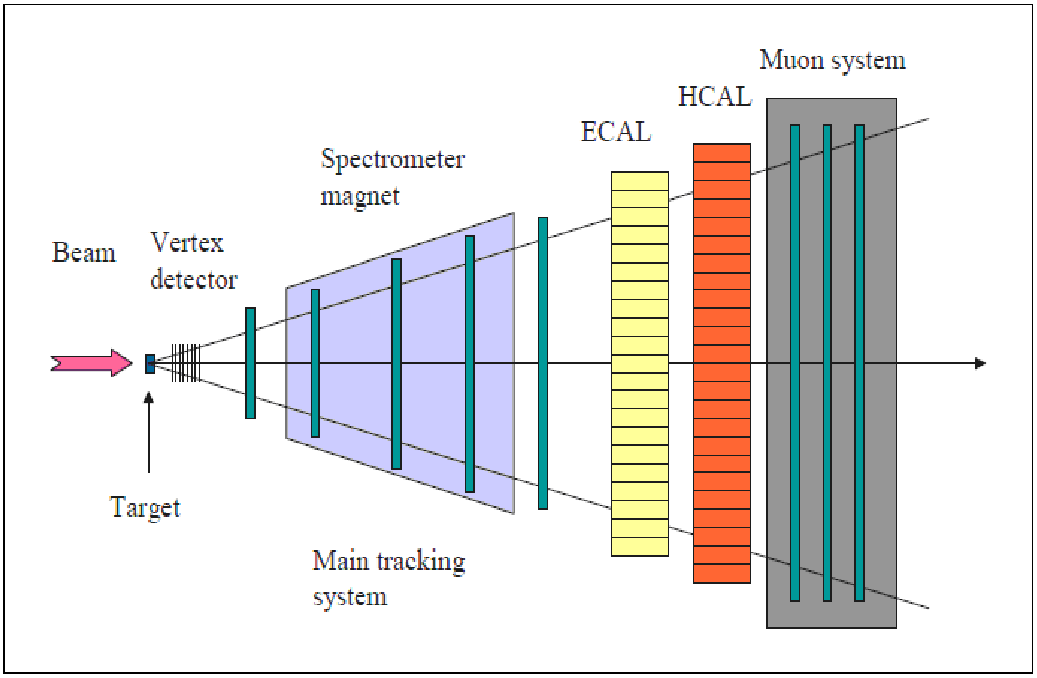

Figure 4.1 : Typical geometry of a forward spectrometer

In the forward geometry, the interaction region lies very often in an area without magnetic field, since the spectrometer magnet is located further downstream. The natural choice of parameters, assuming that the z coordinate points down the spectrometer axis and x and y are the transverse coordinates, is then,

- x_0 the x coordinate at the reference z_0
- y_0 the y coordinate at the reference z_0
- $t_z = \tan\theta_x$ the track slope in the xz plane
- $t_y = \tan\theta_y$ the track slope in the yz plane
- Q/p the inverse particle momentum, signed according to charge

where z_0 denotes the location of a suitable reference plane transverse to the beam, for example at the position of the target, or at the nominal interaction point. The slope parameters allow for a convenient transformation of the parameters to a different reference z value, as is needed during vertex reconstruction. In cases of a very homogeneous magnetic field, it may be advantageous to substitute the parameter Q/p to $Q/p_\perp$, where $p_\perp$ is the momentum in the plane transverse to the magnetic field, or by $\kappa = Q/R$, the signed inverse radius of the curvature.

4.1.2 Collider detector geometry and parameters

Collision between two particles head-on at sufficiently high momentum will require more coverage in terms of particle detection. In general, the detector needs to cover the full solid angle, which leads to a cylindrical detector layout with a solenoid field parallel to the beam axis.

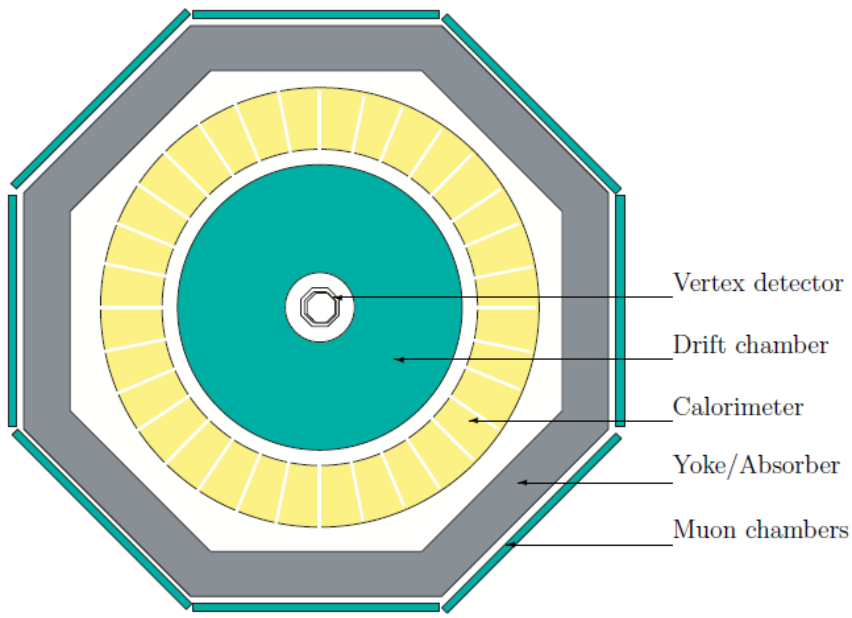

Figure 4.2 : Typical setup of a cylindrical or collider detector.

Somehow at some features, cylindrical geometry comes with different components structure in comparison with the forward geometry detector.

- The vertex detector located at the central part of the detector which is called the barrel part, requires modules parallel to the beam which manage to at least cover the angular acceptance near the interaction point.

- The main tracking system is located within the magnetic field; it generally consist of the coil and yoke of the magnet. The coil is preferably to be located between drift chamber and calorimeter or if possible to make it large enough to enclose the calorimeter.
- To cover full solid angle, the calorimeter will require forward, barrel and rear part.
- The muon detector, the yoke for the solenoid itself readily as absorber.

In collider detectors with cylindrical geometry, the magnetic field normally encompasses the whole tracking volume, including the interaction region where the particles are produced. In a homogeneous solenoid field, the particle trajectory will be a helix curling around an axis parallel to the magnetic field. Assuming the z coordinate is oriented along the detector axis, and the radius is given by $r = \sqrt{x^2 + y^2}$, typical track parameters given at a reference value $r = r_0$ may be

- ϕ_0 the azimuth angle where the trajectory intersects the reference radius
- z_0 the z value where the trajectory intersects the reference radius
- ψ_0 the phase angle of the helix at the reference radius intersection, which corresponds to the angle of the tangent at this point
- Q/R the signed inverse curvature radius of the helix
- $\tan\lambda$ where $\lambda = \arctan p_z / p_\perp$ is the dip angle of the helix

4.2 Parameter estimation

The kinematical parameters of a particle, or also referred to as track fitting parameters, are generally defined as the spatial measurements of a particle flight direction and momentum at its point of origin along the trajectories. To discuss further on this topic, two different methods will be elaborated next.

4.2.1 Least squares estimation

According to least squares estimation, if the trajectory of a particle can be described by a closed expression $f_{\bar{\lambda}}(\ell)$, where λ stands for the set of parameters, ℓ is the flight path and f is the coordinate which could be measured, a set of measurements $\{mi\}$ with errors $\{\sigma_i\}$, will provide an estimate of the parameters, giving

$$X^2 = \sum \frac{(m_i - f_{\bar{\lambda}}(\ell_i))^2}{\sigma_i^2}$$

(29)

If the measurements m_i follow a normal distribution and the function f_λ is sufficiently linear, the expression X^2 will follow a normal distribution. This property can be used for statistical test.

In the case of normally distributed measurements m_i, one can easily convince that the above impression is proportional to the negative logarithm of the corresponding likelihood function, which shows directly the equivalence of least squares principle and maximum likelihood principle for this case.

By denoting the derivative matrix for f as $\frac{\partial f}{\partial \lambda}$, where $\left(\frac{\partial f}{\partial \lambda}\right)_{ij} = \frac{\partial f_{\vec{\lambda}}(\ell_i)}{\partial \lambda_j}$, the symbolizing of this matrix with respect to the parameters as **F** and the (diagonal) error matrix of the measurements as **V** = $diag\{\sigma_i^2\}$**,** the expression to be minimized is

$$(\vec{m} - F\vec{\lambda})^T V^{-1}(\vec{m} - F\vec{\lambda}) \tag{30}$$

and the matrix equation

$$F^T V^{-1}\vec{f} = F^T V^{-1}\vec{m} \tag{31}$$

For linear problem $\vec{f} = F\vec{\lambda}$, the above condition can be directly inverted

$$\vec{\lambda} = (F^T V^{-1} F)^{-1} F^T V^{-1}\vec{m} \tag{32}$$

and the estimated parameters are a linear function of the measurements. The matrix $(F^T V^{-1} F)^{-1}$ is inverted in the shape of $N_\lambda \times N_\lambda$, where N_λ is the number of parameters describing the particle.

Meanwhile, the covariance matrix of the parameter estimate can be directly determined as

$$\mathrm{cov}(\vec{\lambda}) = C_\lambda = (F^T V^{-1} F)^{-1} \tag{33}$$

The least squares method is popular due to its optimality properties of linear case as follow,

- The estimate is unbiased, for instance, the expectation value of the estimate is the true value
- The estimate is efficient, whereby, of all unbiased estimates which are linear functions of the observables, this method has the smallest variance which is generally called the Gauss-Markov-Theorem.

In fact, in most cases where the function $f_{\vec{\lambda}}$ can be locally approximated by a linear expansion, these properties are still retained.

4.2.2 The Kalman Filter Technique

Different from the least squares parameter estimation which requires the global availability of all measurements at fitting time, the Kalman filter technique was developed to determine the trajectory of the state vector of a dynamical system from a set of measurements taken at different times. In considering cases such as in real-time tracking of objects, or in pattern recognition scheme which are based on track following, where it is not clear a-priori if the hit combination under consideration does really belong to an actual track, the Kalman filter technique is more convenient for estimating the measurements compared to the first method.

The Kalman filter technique efficiently improves track and vertex reconstruction based on two steps. Firstly in the prediction step, an estimate is made for the next measurement from the current knowledge of the state vector, where it is very useful to discard noise signals and hits from other tracks from the fit. Secondly in the filter step, the updates of the state vector does not require inversion of a matrix with dimension of the state vector as in a global fit, but only with the dimension of the measurement.

To describe Kalman filter in this thesis, implementation and nomenclature from [39-41] is referred. In this notation, the system state at the time, after inclusion of k measurements is denoted by $\tilde{x}_k$, its covariance matrix by C_k. $\tilde{x}_k$ contains the parameters of the fitted track, given at the position of the k^{th} hit. The matrix F_k describes the propagation of the track parameters from the $(k-1)^{th}$ to the k^{th} hit. For example, in a planar geometry with one-dimensional measurements and straight line tracks, the propagation takes the form

$$\begin{pmatrix} x \\ t_x \end{pmatrix}_k = \begin{pmatrix} 1 & z_k - z_{k-1} \\ 0 & 1 \end{pmatrix} \begin{pmatrix} x \\ t_x \end{pmatrix}_{k-1} \qquad (34)$$

where a subset of the track parameterization in section 4.1.1 has been used. The coordinate measured by the k^{th} is denoted by m_k. In general m_k is a vector with the dimension of that specific measurement. For tracking devices measuring only one coordinate, m_k is an ordinary number. The measurement error is described by the covariance matrix V_k. The relation between the track parameters $\tilde{x}_k$ and the predicted measurement is described by the projection matrix H_k. In the example in section 4.3.2, the measured coordinate in the stereo view u is

$$H\begin{pmatrix} x \\ y \end{pmatrix} = \left(\cos\alpha_{st} \ -\sin\alpha_{st}\right)\begin{pmatrix} x \\ y \end{pmatrix} \tag{35}$$

with α_{st} as the stereo angle at 45°.

In each filter step, the state vector and its covariance matrix are propagated to the location or time of the next measurement with the prediction equations,

$$\tilde{x}_k^{k-1} = F_k \tilde{x}_{k-1}, \qquad C_k^{k-1} = F_k C_{k-1} F_k^T + Q_k \tag{36}$$

and the estimated residual becomes,

$$r_k^{k-1} = m_k - H_k \tilde{x}_k^{k-1}, \qquad R_k^{k-1} = V_k + H_k C_k^{k-1} H_k^T \tag{37}$$

Here Q_k denotes the additional error introduced by process noise, such as random perturbations of the particle trajectory, for example multiple scattering. The updating of the system state vector with the k^{th} measurement is performed wit the filter equations,

$$K_k = C_k^{k-1} H^T \left(V_k + H_k C_k^{k-1} H_k^T\right)^{-1}$$

(38)

$$\tilde{x}_k = \tilde{x}_k^{k-1} + K_k\left(m_k - H_k \tilde{x}_k^{k-1}\right)$$

$$C_k = \left(1 - K_k H_k\right) C_k^{k-1}$$

with the filtered residuals

$$r_k = \left(1 - H_k K_k\right) r_k^{k-1} \qquad R_k = \left(1 - H_k K_k\right) V_k \tag{39}$$

K_k is sometimes called the gain matrix. The χ^2 contribution of the filtered point is then given by

$$\chi^2_{k,F} = r_k^T R_k^{-1} r_k \tag{40}$$

The system state vector at the last filtered point always contains the full information from all points. If one needs the full state vector at every point of the trajectory, the new information has to be passed upstream with the smoother equations,

$$A_k = C_k F_{k+1}^T \left(C_{k+1}^k\right)^{-1}$$

(41)

$$\tilde{x}_k^n = \tilde{x}_k + A_k\left(\tilde{x}_{k+1}^n - \tilde{x}_{k+1}^k\right)$$

$$C_k^n = C_k + A_k\left(C_{k+1}^n - C_{k+1}^k\right)A_k^T$$

$$r_k^n = m_k - H_k \tilde{x}_k^n$$

$$R_k^n = R_k - H_k A_k\left(C_{k+1}^n - C_{k+1}^k\right)A_k^T H_k^T$$

Thus, smoothing is also a recursive operation which proceeds step by step in the direction opposite to that of the filter. The quantities used in each step have been calculated in the preceding filter process. If process noise is taken into account, for example to model multiple scattering, the smoothed trajectory may in general contain small kinks and thus reproduce more closely the real path of the particle.

In the equation above, F and H are just ordinary matrices if both transport and projection in measurement space are linear operations. In the case of non-linear systems, they have to be replaced by the corresponding functions and their derivatives,

$$F_k \tilde{x}_k \rightarrow f_k(\tilde{x}_k) \qquad\qquad H_k \tilde{x}_k \rightarrow h_k(\tilde{x}_k) \tag{42}$$

using for covariance matrix transformations

$$F_k \rightarrow \frac{\partial f_k}{\partial \tilde{x}_k} \qquad\qquad H_k \rightarrow \frac{\partial h_k}{\partial \tilde{x}_k} \tag{43}$$

The dependence of f_k and h_k on the state vector estimate will in general require iteration until the trajectory converges such that all derivatives are calculated at their proper positions.

4.3 Typical tracking devices

4.3.1 Single-coordinate measurement

When a particle traverses tracking devices leaving a single coordinate at specific location, the mechanism of measurement will be different depending on the tracking component. As for tracks nearer to the interaction point, in particular solid-state detector such as vertex detectors and micro-vertex detector, the device used is similar to the strip detector concept which using semiconductor-based strips as a widespread type of tracking device. Meanwhile for tracks which slightly far from the central point, sense wires are chosen to detect the track signal within the gaseous chamber.

4.3.1.1 *Silicon Strip detector*

The silicon strip detector is a semiconductor-based device structured in strips with widths about 25 μm each. Smaller width can give better precision of the particle trajectories, for instance micro-vertex detector strips are with widths down to 10 μm. Each strip is functioning like a small diode, allowing voltage to get through such that the border between the strips is depleted eventually producing a high resistance volume. When a charged particle traverses the strip plane, pairs of electrons and corresponding holes will be created, which will then be isolated by the voltage and registered as a pulse. The pulse height can be measured by a suitable clustering algorithm, for example centre-of-gravity based, and determines the location passed by the traversing particle. Solid-state detectors are presently the tracking devices with the highest spatial resolution which improve the reconstruction of primary and secondary vertices. Moreover, they are very good to protect against radiation damage. Despite these advantages, solid-state detectors are still unaffordable to be implemented for whole detector volumes as they are presently very expensive.

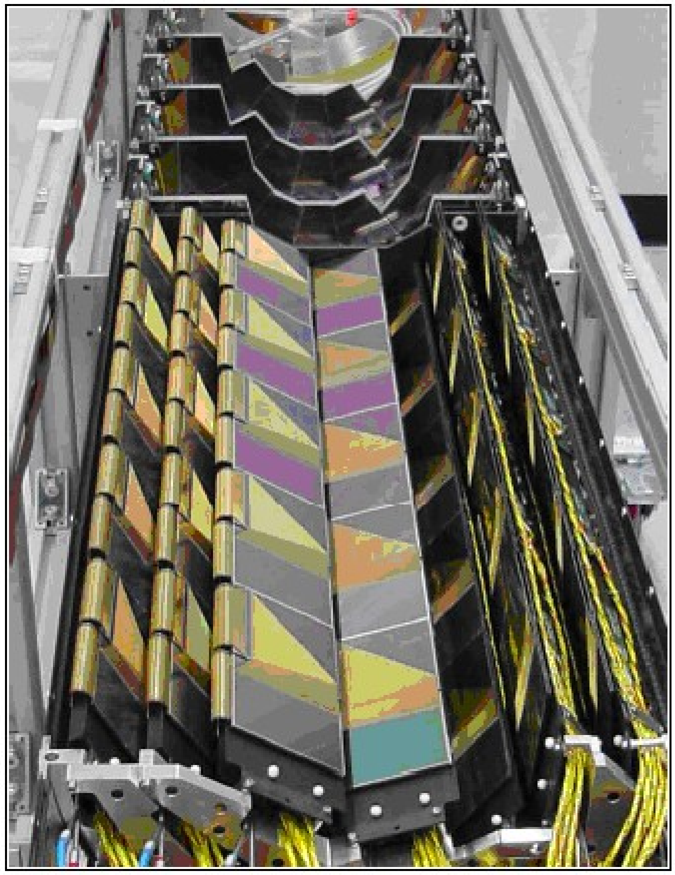

Figure 4.3 : Lower half barrel of the ZEUS micro-vertex detector

4.3.1.2 *Drift chambers*

With significantly large areas to be covered, the gaseous or drift chamber is the most suitable tracking device. To determine the momentum of the traversing particle, the particle need to move within a magnetic field, and the particle tracks will subsequently provide the leverage that determines the precision of momentum reconstruction. As to that reason, the drift chamber maintains as the largest component in tracking volume.

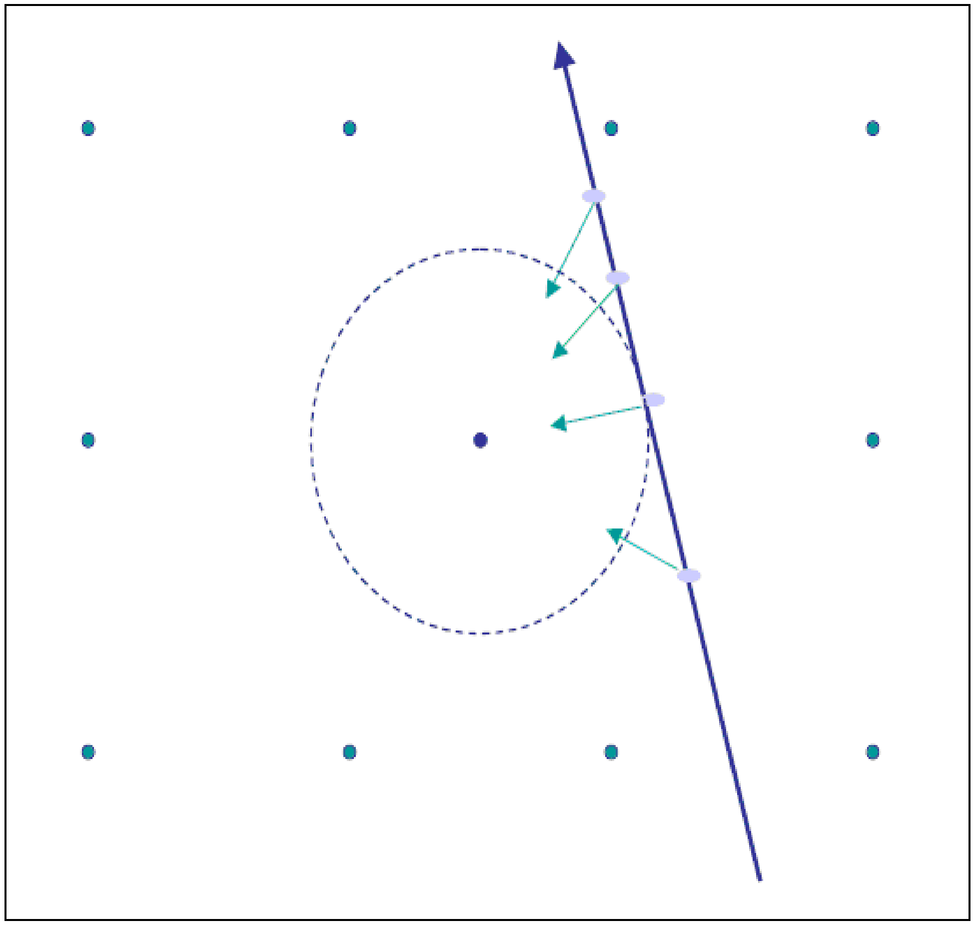

Figure 4.4: Schematic view of a drift chamber cell. The closed circle indicates wires, with sense wires in the middle and field wires on the outside. The long and thick arrow represents a trajectory of a particle while the small arrows denote primary ionization charges drifting towards the sense wire.

A drift cell consists of a sense wire or in particular an anode wire in the middle and is surrounded by field wires at the edge. The cell shape is not necessarily rectangular, but adjustable to any other convenient design. Primary ionization occurs along the particle trajectories leaving free charges which subsequently drift to the nearest sense wire. A large number of particles near the sense wire will result a multiplication of ionization which is called gas amplification within a large electric field. The rising entries of signal pick up by the anode wire triggers a time-to-digital converter (TDC) which then measures the time until a common stop signal. Then, the system will measure the drift time of those charges which are considered as the first to arrive. Generally, in the case of there being more than one particle trajectory at a time in a same drift cell, only the nearest track to the wire will be registered. Also, the single measurement is unable to distinguish which side the particle traverses, resulting in an uncertainty called the left-right ambiguity. Moreover, in the worst case, the left-right ambiguity will produce a mirror track which cannot be distinguished from the real one. However, presently there are better designs developed to overcome this problem.

Drift in gases is influenced also by magnetic field. The deviation of the gas drift direction from the vector of the electric field is described by the Lorentz angle. Figure 4.5 shows an event display of the central tracking detector (CTD) of the ZEUS experiment, in the view along the beam axis. The view was taken using a graphic software tool in the ROOT event display. The Lorentz angle in this example is 45° and it is reflected in the design of the cell structure.

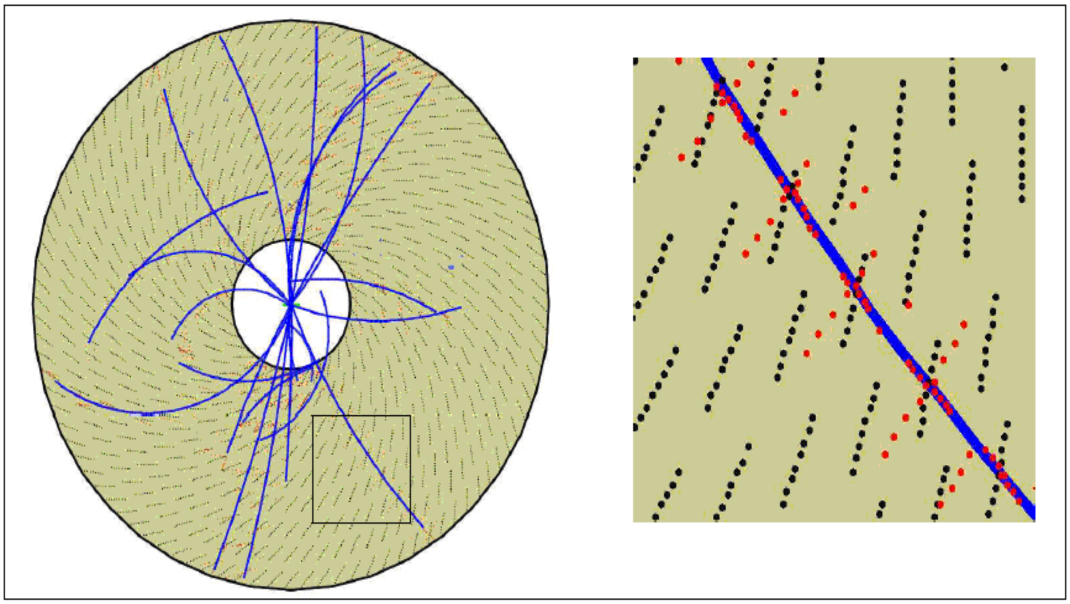

Figure 4.5: Event display from the ZEUS central tracking detector where the closeup view is given in the square. The blue line is the trajectory and the red dot is the drift distance end points on both side of the corresponding wire.

4.3.2 Stereo angle

Single-coordinate measurement is only limited for single trajectory within a projected space but not providing any 3-Dimensional views. Hence, to create a three axial views, several projected space need to be combined, which typically known as stereo views. In several cases which more than one track involved, ambiguities may occur to locate the exact intersection points of the particles where the real points will be seen having a pair. These pairs which commonly recognized as ghost points will create ambiguities in the measurement.

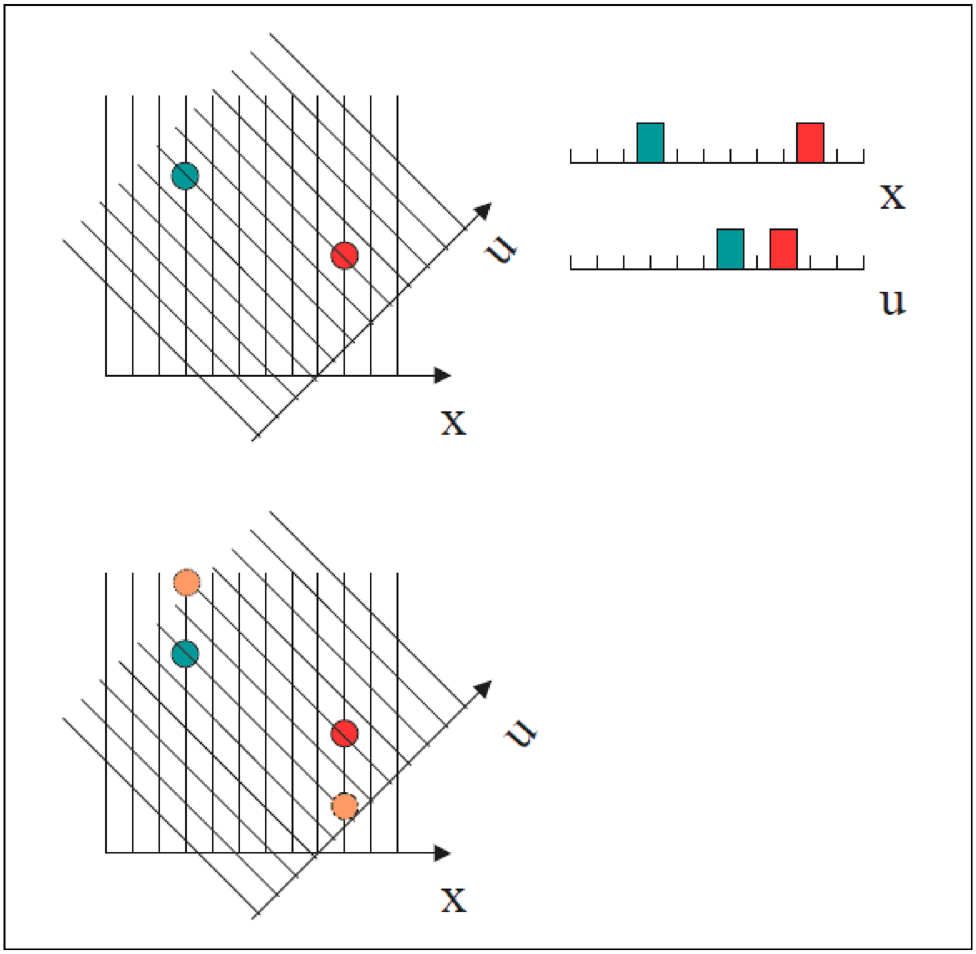

Figure 4.6 : Top left : The real hit points with two stereo views on x plane (0°) and u plane (45°). Top right : Single view on x and u plane with two ghost points in blue. Bottom left : Ambiguity hits observed on x and u plane.

Figure 4.6 shows two particle intersection on two strip detector x and u. In this case, since the true tracks are well separated, the uppermost ghost combination is already just outside the chamber acceptance of the u view. This concept is called an all-stereo design. Ambiguities of the assignment of the measured hits in the x and u views to each other lead to the reconstruction of two ghost points. In general at least three views are necessary to avoid this kind of ambiguities. Usage of more than one measurement concepts in detector design, in general are currently implemented to maximise particle detection capabilities of the detector as well as due to economic reasons.

4.3.3 Three-Dimensional (3D) measurement

Better precision measurement and higher efficiency in avoiding ghost points are the main advantage of using 3-dimentional views. Not only for solid-state detector, 3-dimentional measurement can also be applied to gaseous detector, where the examples can be observed in CCD-based vertex detector in SLD experiment and the TPC in STAR experiment [38]. In 3D views for gaseous chamber, no wires are used, but an electrode membrane is located at the middle plane in axial electric field to drift charges to the anode and be registered.

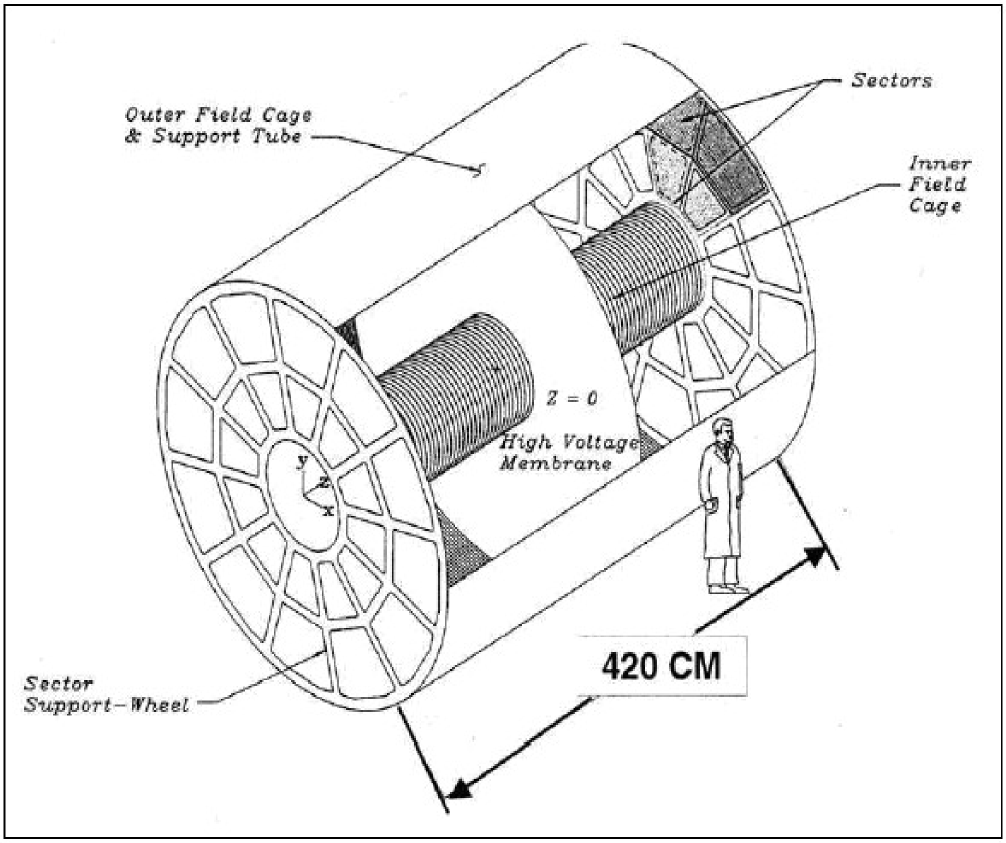

Figure 4.7 : TPC of the STAR experiment.

4.4 Performance Evaluation

4.4.1 The reference set

Tracks are normally provided by a Monte Carlo simulation and the selection of reference tracks usually depends on the physics motivation of the experiment. However, tracks are disregarded and excluded due to the following reasons,

- Low momentum particles arising from secondary interactions in the material
- Particles traveling outside the geometrical acceptance, for example trajectories within the beam hole of a collider experiment cannot be traced by the detector
- Particles straddling the border of a detector and traversing only a small number of tracking layers. To be regarded as constituents of reference set, particles need to traverse at least 80% of the nominal tracking layers.

The definition of the reference set can be referred as a definition of effective geometrical acceptance

$$\in_{geo} = \frac{N_{ref}}{N_{total}} \tag{44}$$

with N_{ref} and N_{total} denoting the numbers of particles of interest in the reference set and in total, respectively.

4.4.2 Track finding efficiency

To evaluate whether a track has been effectively identified or found by the algorithm or not, two different concepts are typically used as benchmarks. Tracks are observed by,

- Hit matching. By using the Monte Carlo truth information, this method analyzes the simulated origin of each reconstructed hit in the reconstructed track. If the qualified majority of hits are at least 70% originates from the same true particle, the track is said to reconstruct this particle. This method is stable in the limit of very high track densities, but requires the Monte Carlo truth information to be mapped meticulously through the whole simulation.
- Parameter Matching. The reconstructed parameters of a track are compared with the true particles. Although this method requires less functionality from the simulated chain, it bears the danger of accepting random coincidence between true particles and artifacts from pattern recognition algorithm.

The reconstruction efficiency can be defined as,

$$\in_{reco} = \frac{N_{ref}^{reco}}{N_{ref}} \tag{45}$$

where N_{ref}^{reco} is the number of reference particles that are reconstructed by at least one track. Otherwise for the abundance of non-reference tracks which are reconstructed, $N_{non-ref}^{reco}$ the relation is,

$$\frac{N_{non-ref}^{reco}}{N_{total} - N_{ref}} << \in_{reco} \tag{46}$$

4.4.3 Ghosts

Ghosts are defined as the tracks produced by pattern recognition algorithm which does not reconstruct any true particles within or without the reference set. A ghost rate can be calculated by,

$$\in_{ghost} = \frac{N_{ghost}}{N_{ref}} \tag{47}$$

where N_{ghost} is the number of ghosts.

The mean number of ghosts per event can also be specified since the ghost rate may be dominated by a small subset of events with copious hit multiplicity.

4.4.4 Clones

'Clones' is another term we use to analyze redundant reconstruction of particles. The number of clone can be determined by,

$$N_m^{clone} = N_m^{reco} - 1 \quad \text{if} \quad N_m^{reco} > 0 \tag{48}$$

and otherwise,

$$N_m^{clone} = 0 \tag{49}$$

where m is the given particle and N_m^{reco} is its number of reconstructed tracks for m.

Hence, the clone rate is

$$\in_{clone} = \frac{\sum_m N_m^{clone}}{N_{ref}} \tag{50}$$

4.4.5 Parameter resolution

Physics performance in an experiment is extremely dependent on the quality of reconstructed particle parameters and error estimates from the reconstruction in the detector components. Thus the parameter residual of a track parameter X_i can be defined as

$$R(X_i) = X_i^{rec} - X_i^{true} \tag{51}$$

where X_i^{rec} and X_i^{true} are the reconstructed and true track parameter respectively.

Form equation above, the parameter estimate bias $\langle R(X_i) \rangle$, can be obtained. By using the estimate of the parameter covariance matrix, C_{ii} , the normalized parameter residual can be defined as

$$P(X_i) = \frac{X_i^{rec} - X_i^{true}}{\sqrt{C_{ii}}} \tag{52}$$

CHAPTER 5

DATA ANALYSIS AND RESULTS

5.1 ORANGE (Overlying Routine Analysis of Ntuple Generation)

ORANGE [42] is a standard analysis tool in a standard analysis environment which had been created and implemented to enhance the analysis structure at DESY since 1999. In order to overcome some issues of data disarrangement, linking and updating, ORANGE was created as a solution introducing a systematic data handling with specific system flows and structures. In ORANGE, there are routines and subroutines available for different kind of analysis which referred to specific events or components of the detector. One can pre-select the information that is needed using control cards and generate the data accordingly. Back then, one needed to edit their own control cards to produce data, however after the new initiative of grand reprocessed data, the data have already been prepared accordingly and are ready to be used by the end user. More on grand reprocessed data will be discussed in the coming section 5.3. Figure 5.1 shows the example of control cards for an analysis done in 2005. Data entries for the routines selected then will be processed and gathered in specific data files in the form of ntuples.

```
C
C          Orange Control Cards
C       version 2005a from 05.06.2005
C
C Enable ORANGE
OREAZE-ENABLE ON
C ==========================================================
C Switches and paramters for each of the major code sections
C These cards determine which ORANGE common blocks are filled
C and also how they are filled. To determine which common blocks
C are written to the ntuple, see the ORANGE-NTBLOCKS cards below
C ==========================================================
C
C Fill trigger information
ORANGE-TRIGFILL ON
C
C Collect information for diffractive analyses
ORANGE-DIFFFILL OFF
C
C ======= JET FINDING ========
C Jet finding master switch
ORANGE-JETSFILL ON
C
C Cone jet finding algorithm
ORANGE-CONEJET ON
C mode 0=CAL cells, 1=zufos, 2=hadron level, 3=cone islands, 4=CAL+FPC cells
ORANGE-CONEMODE 0
ORANGE-CNETAMIN -2.0
ORANGE-CNETAMAX 3.2
ORANGE-CNPTMIN  2.5
ORANGE-CNSEED   0.5
ORANGE-CNRCONE  1.0
C 0=no ele rejection, 1=rej EM ele, 2=rej Sira ele
ORANGE-CNEREJ   1
C
C KT jet finding algorithm
C Four finders A,B,C,D, each fully variable, but with a
C different set of defaults (see manual).
ORANGE-KTJETSA ON
```

Figure 5.1 : Example of initial page of control cards which show selection of several routines applicable in ORANGE.

5.2 Data Analysis Software

5.2.1 Physics Analysis Worstation (PAW)

PAW is an interactive utility for visualizing experimental data on a computer graphics display. It may be run in batch mode if desired for very large and time consuming data analyses; typically, however, the user will decide on an analysis procedure interactively before running a batch job. PAW combines a handful of CERN High Energy Physics Library systems that may also used individually in software that processes and displays data. The purpose of PAW is to provide many common analysis and display procedures that would be duplicated needlessly by individual programmers, to supply a flexible way to invoke these common procedures, and yet also to allow user customization where necessary. Thus, PAW's strong point is that it provides quick access to many facilities in the CERN library. One of its limitations is that these libraries were not designed from scratch to work together, so that a PAW user must eventually become somewhat familiar with many dissimilar subsystems in order to make effective use of PAW's more complex capabilities. As PAW evolves in the direction of more sophisticated interactive graphics interfaces and object-oriented interaction styles, the hope is that such limitations will gradually become less visible to the user.

In ORANGE analysis, PAW will be used as an interpreter for the processed data. The data which has been processed by ORANGE can be plotted and execute by PAW using its programming language, FORTRAN. As interactive software, PAW will recognize the routine in ORANGE and display the data in a table called the ntuple blocks. If the network traffic can be tolerated, PAW can be run remotely over the network from a large, multi user client machine to more economical servers such as an X-terminal. In case such facilities are unavailable, substantial effort has been made to ensure that PAW can be used also in non interactive or batch mode from mainframes or minicomputers using ASCII terminals. Figure 5.2 shows the components of PAW with its functions.

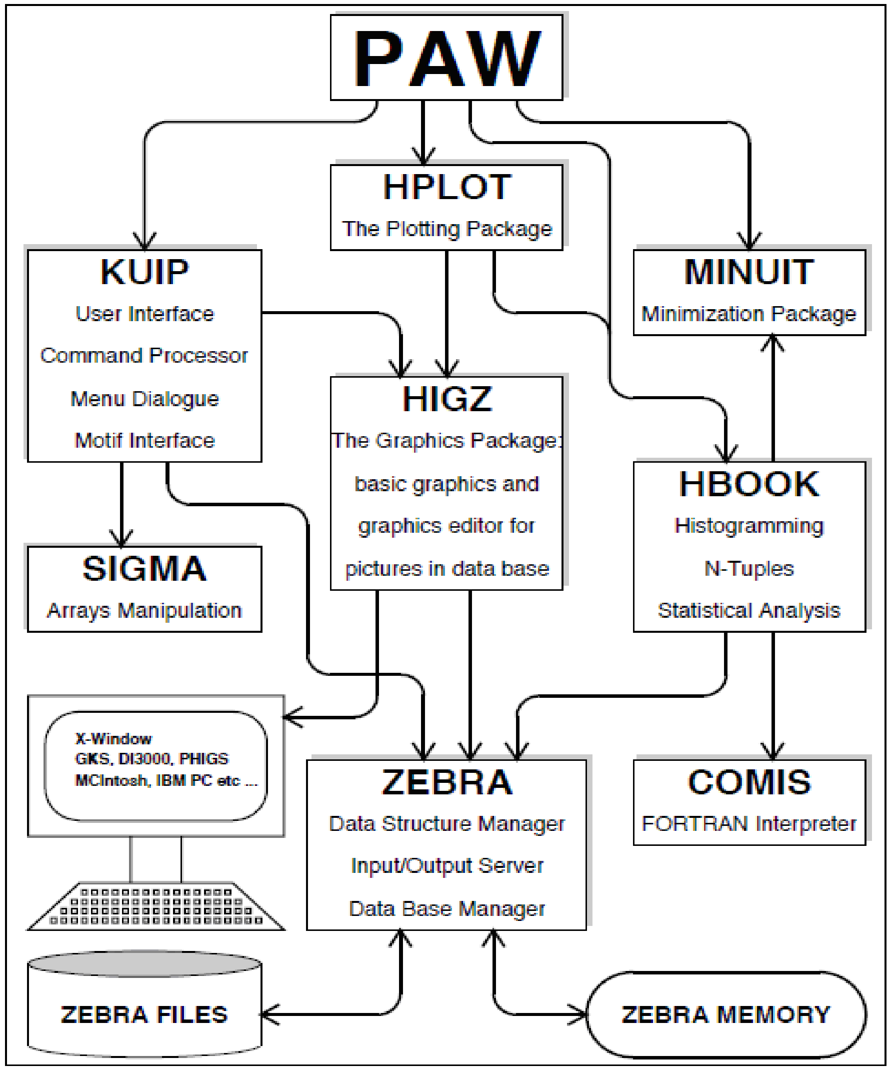

Figure 5.2: PAW and its components

5.2.2 ROOT

ROOT is another software analysis used at ZEUS which is familiar with ORANGE routines. Compared to PAW, ROOT is a newer data processing technology which was introduced by CERN through its experiment called the NA49. The objective of ROOT development is to build software that can generate and process bigger amount of data up to 10 Tb per run. Rough comparison between PAW and ROOT is listed in Table 1.0. As new enhanced and modern software of data analysis, ROOT provides platform independent access to a computer's graphics subsystem and operating system using abstract layers. Parts of the abstract platform are such as a graphical user interface and a GUI builder, container classes, reflection, a C++ script and command line interpreter (CINT), object serialization and persistence. In ZEUS analysis, ROOT plays the same function as PAW. Using specific command, ORANGE data can be linked and displayed in ROOT interface. The format of the data is also supported by ROOT and can be executed using CINT. Figure 5.3 shows the main systems in ROOT with its specific routines and executing files.

Table 1.0 : Rough comparison between PAW and ROOT.

	PAW	**ROOT**
Developers	CERN	CERN
Stable Release	16-Sep-02	22-Sep-11
File Format	.ntp	.root
Type	Particle Physics	Data Analysis
Programming Language	Fortran	C++

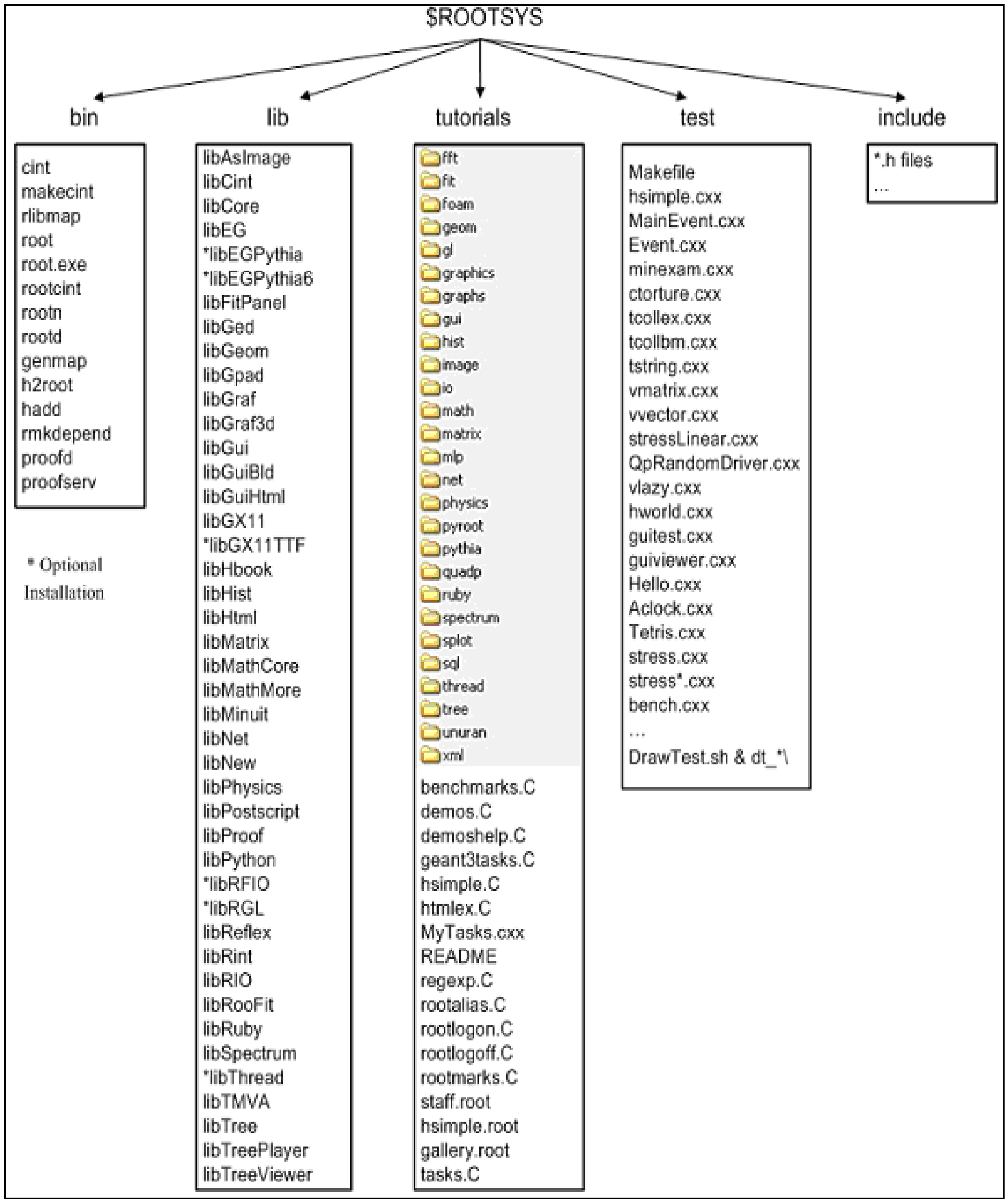

Figure 5.3: ROOT framework directories

5.2.3 Zeus Event Visualization (ZEVIS)

After installation of new components (MVD and STT) for HERA II, there was a challenge in event display as the available software at that time was not maintainable and portable to the new platforms. Therefore, ZEVIS was developed and introduced with better resolution and specifications as listed below,

- New facilities with integrated display of 2-Dimentional and 3-Dimentional view
- Portability, able to support available and relevant ZEUS software platforms
- Modality, able to use display without direct data access.

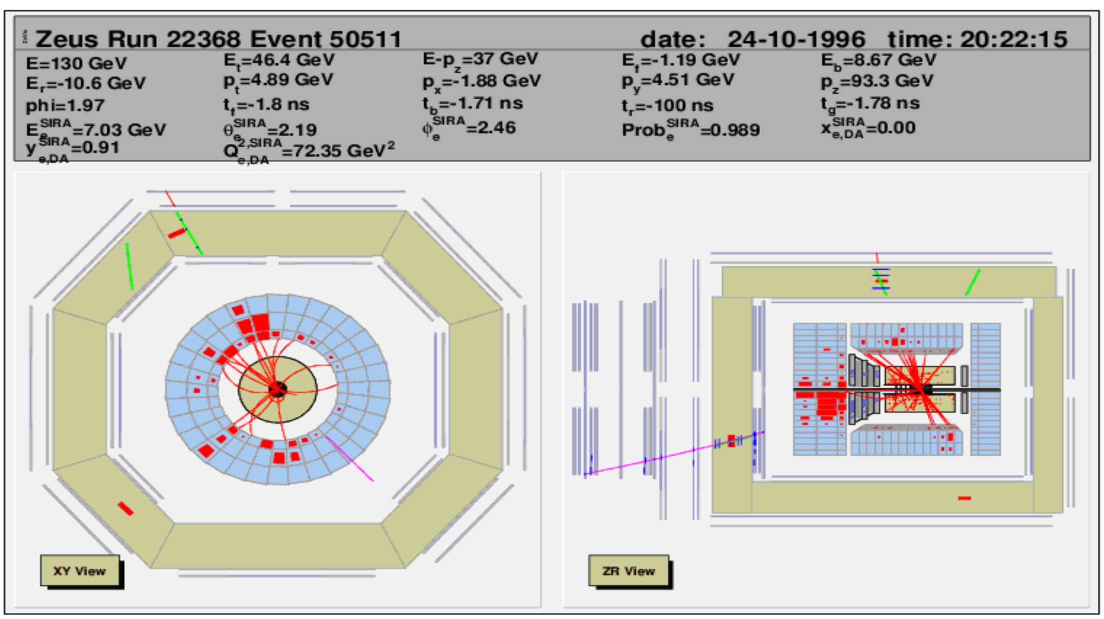

Figure 5.4: ZEVIS display of trimuon event. One of the muons is identified in the outer barrel muon chambers and in BAC (both hits and pads), embedded into a jet. The second is seen in BAC only (pads only).The third is seen in the forward muon chambers (clean long track starting in the inner chambers) and in the forward BAC, embedded into a forward jet.

5.3 Grand Reprocessed (GR) Data

In the middle of 2007, HERA operation had been stopped. Since its launch, a huge amount of data has been collected. Until 2011, the ZEUS collaboration is confident that the infrastructure of data processing in ZEUS system can be well maintained. However, beyond that year, they are uncertain whether this infrastructure can be preserved. To overcome such impact, the collaboration has come up with the idea of general data set or ntuple production called the GR data. Thus, these GR ntuples are useful for all kind of analysis and can be easily preserved for future reference and research. The first step of GR data production had been done in 2006. Now, after nearly 5 years of development, the collaboration has succeeded to produce GR ntuples of millions events in real data and Monte Carlo (MC) starting from running year 2003 to 2007 in various versions. The latest versions are v05 and v06 which still under development and construction. There are two file formats for GR data to support two common offline analysis softwares at ZEUS which are PAW and ROOT.

5.4 Monte Carlo (MC) Data

To evaluate the reconstruction of particle in real data, Monte Carlo (MC) simulation is used as comparison. At ZEUS, there are several MC generators available for different interactions. For exclusive vector meson production, the DIFFVM generator is used. The mechanism of DIFFVM simulation is based on

Regge Phenomenology and Vector Dominance Model (See Section 3.9). When electron collides with proton at high energy, the electron will emit a photon which subsequently fluctuates into a vector meson.

The steps of the MC simulation process are listed below:-

- Physics generator. This is a program that generates events coming from the reaction $ep \to X$. Each event consists of a table of the four momenta of all the particles involved in the reaction: incoming, intermediate and final state.

- MOZART (MOnteCarlo for ZEUS Analysis, Reconstruction and Trigger) is a software that contains the full simulation of the ZEUS detector. The interaction of particles with the various components of the ZEUS detector is simulated by GEANT package. The geometrical and material structure of components of the ZEUS detector as well as the mapping of the magnetic field in the volume of the CTD is known to MOZART. The program produces two types of tables, the table that contains the full information of all particles created in the event and the tables that contain the output of the various components of the ZEUS detector.

- ZGANA (ZG313 ANAlysis). This is a program that simulates the three-level trigger of the ZEUS detector as available at the various trigger levels.

- Once the generated MC file has been processed through the steps enumerated it is ready to go through the event reconstruction by the program ZEPHYR. After this the MC file undergoes the same off-line treatment as data.

These steps can be viewed in simpler diagram as shown in Figure 5.5.

Comparison of GR data and MC data in term of ntuple volume is shown in Table 2.0. From this figure, we can see that the volume of MC data generated is bigger than the GR data as more simulation has been done to ensure all events scenarios are captured for reference.

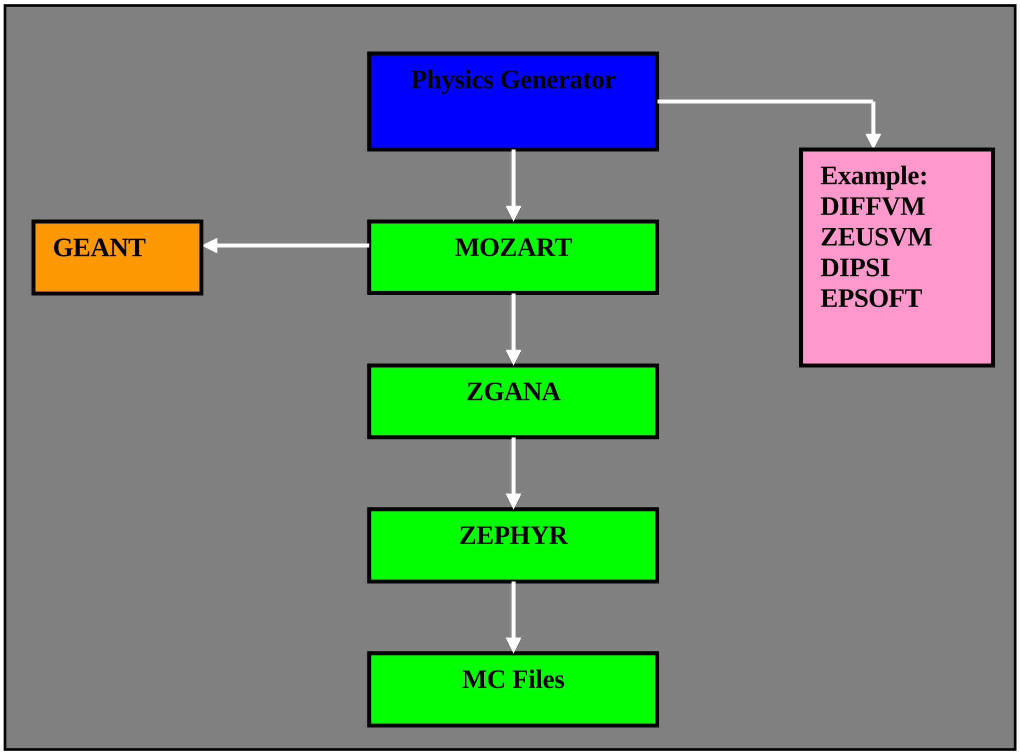

Figure 5.5: Steps of Monte Carlo Simulation

Table 2.0 : Size of GR ntuple for v02 and v04.

VERSION	TYPE	EVENTS	PAW	ROOT
v02d	DATA	410M	1.9TB	3.0TB
v02e	MC	660M	14.0TB	6.6TB
v02f	MC	477M	2.4TB	5.6TB
v04b	DATA	410M	4.4TB	5.0TB
v04b	MC	208M	4.7TB	3.0TB
v04b	MC	1137M	25.7TB	16.3TB

5.5 ψ' Photoproduction (PHP)

The production of particle that originates from photon is called the photoproduction (PHP). Photon can be seen either exclusively or inclusively in the interaction. ‘Exclusive’ means the photon is produced exclusively from the first interaction of the proton and electron. Meanwhile, ‘inclusive’ means the photon is produced within the interaction which may or may not come from the incident electron or proton itself.

In this analysis of ψ' PHP, some significant aspects of the analysis should be noted. The exclusivity of the events has to be the most important aspect, whereby, in each event, the number of tracks for charged particles must be exclusively similar with the search particle decay products. In the interaction of $\psi' \rightarrow J/\psi\pi^+\pi^-$ there will be exactly 4 tracks which represent 2 muons (from J/ψ decay) and 2 pions. The offline selection will involve specific parameters from a data arrangement table in GR data, called the ntuple blocks which can be viewed using the software analysis PAW or ROOT. All of ORANGE routine are listed in this table with its specific parameters. These parameters are used or called in PAW or ROOT using the software recognized command language and can be executed in a program.

The offline selections for $\psi' \to J/\psi\pi^+\pi^-$ PHP are listed as following;

- Exclusively 4 tracks which consist of 2 tracks of muons and 2 tracks of pions. These particles must be distinguished correctly base on the ID to prevent overlapping between particles and must have a correct charges. Entries of muons are taken from the GMUON routine in the ntuple block which is measured by the muon detector. Meanwhile for pions, the TRACKING routine used where particles entries are measured by tracking detector i.e CTD, MVD.

- The newest routine track type ZTTRACK is chosen. This routine can be viewed in the ntuple block. For GR data, the track type has already been set to this routine.

- The interaction area must cover in the primary vertex region. This is done by setting the zvtx within the 50cm. zvtx parameter is listed under the TRACKING routine in ntuple blocks.

- The polar angle for muon pairs are set to be within $17^\circ < \theta < 163^\circ$, in the region of CTD acceptance. The θ parameter is listed under GMUON routine in ntuple blocks.

- Collinearity cut for J/ψ, $\Omega < 174^{\circ}$, where Ω is the angle between the two muon tracks to reject cosmic rays events. The formula used for this cut is $\cos\Omega = \frac{-P_i \bullet P_j}{|P_i||P_j|}$ where P_i is the momentum x,y and z for muon i and P_j is the momentum x,y and z for muon j. The parameters for these momentum also can be obtained from the ntuple blocks under the GMUON table.

- The J/ψ mass reconstruction, $M_{J/\psi}$ are cut within a small region around the mass peak to decrease the background.

- Trigger selection for FMUON/BRMUON are applied.

ψ' Mass reconstruction is calculated using equation below,

$$M_{\psi(2S)} = M_{\mu^+\mu^-\pi^+\pi^-} - M_{\mu^+\mu^-} + M_{J/\psi}(PDG) \tag{53}$$

where $M_{\mu^+\mu^-\pi^+\pi^-}$ is the reconstructed mass for $\psi(2S)$ using 2 muons and 2 pions, $M_{\mu^+\mu^-}$ is reconstructed mass for J/ψ and $M_{J/\psi}(PDG)$ is the mass value for J/ψ in particle data group (PDG) reference. This formula is used to confirm the accuracy of the ψ' reconstructed mass which must be balanced with the value in the PDG. After ψ' reconstructed signal is observed in the plotted graph, to obtain the number of ψ' entries in the mass region $N_{\psi(2S)}$, some fitting algorithm are used i.e Gaussian. This fitting routine option is also available in PAW and ROOT.

5.6 Results

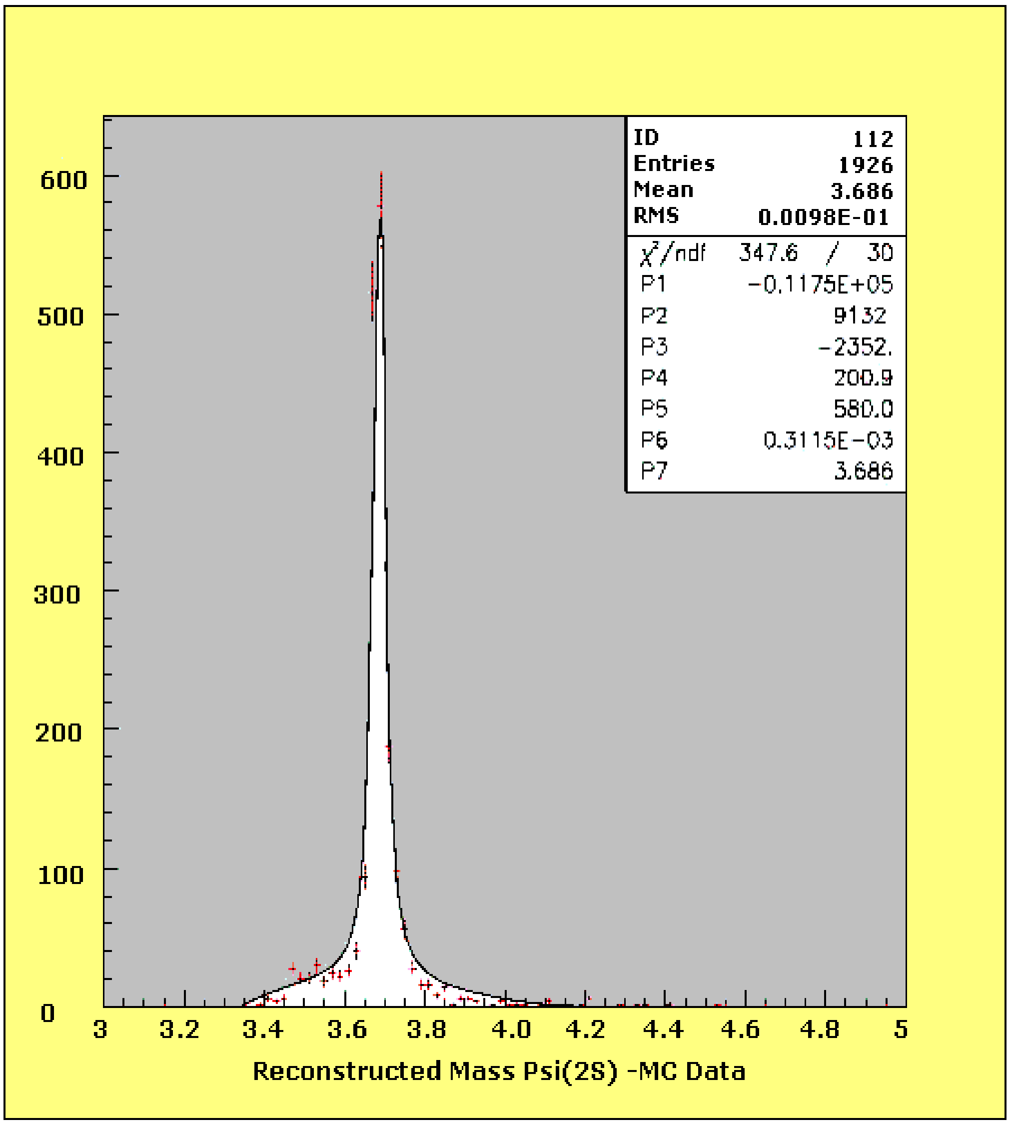

Figure 5.6: Figure shows the reconstructed mass of ψ' generated by PAW using the simulated ZEUS MC data for $\psi' \rightarrow J/\psi\pi^{+}\pi^{-}$ decay channel.

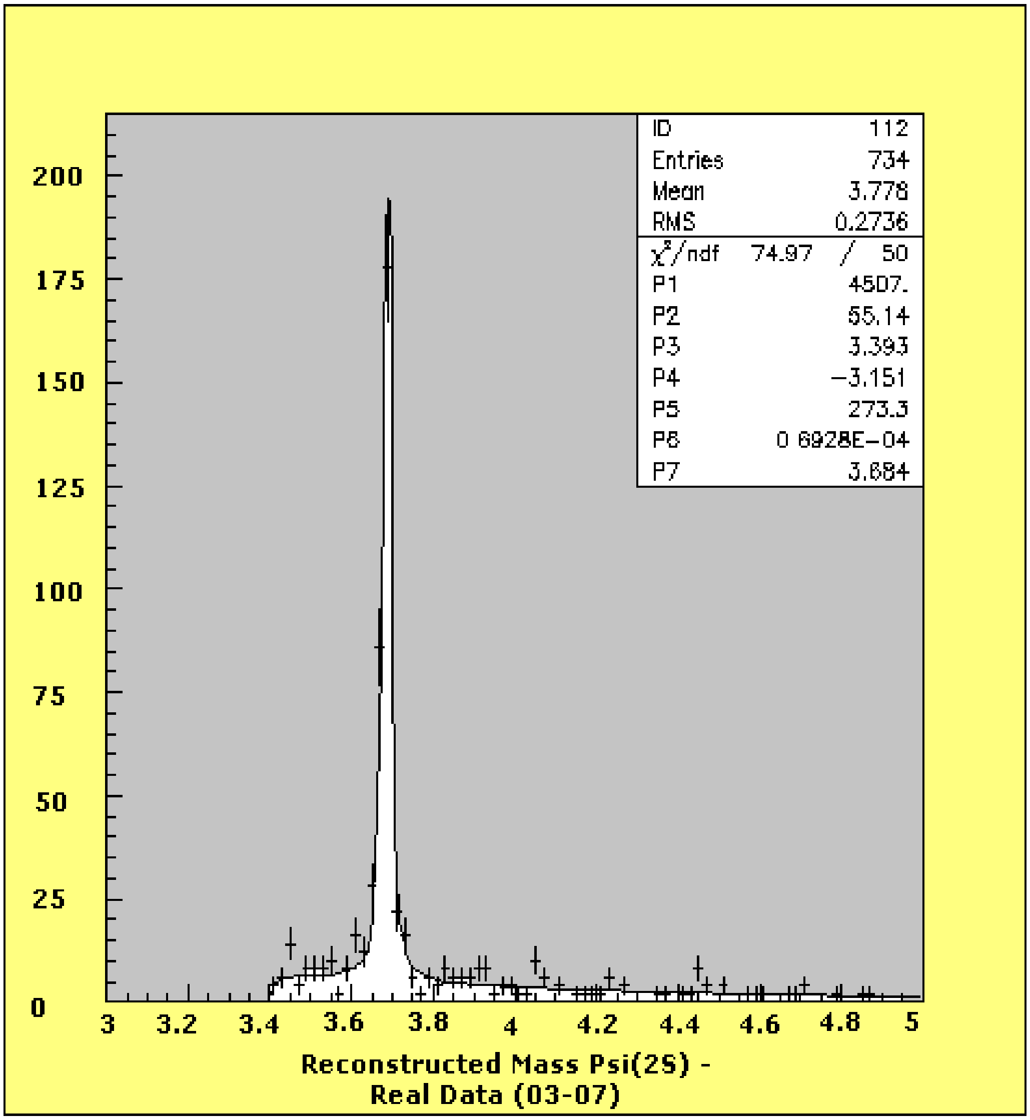

Figure 5.7: Figure shows the reconstructed mass of ψ' generated by PAW using the ZEUS GR data for $\psi' \rightarrow \mu^+\mu^-\pi^+\pi^-$ decay channel in 2003-2007 events.

Table 3.0: Properties of ψ' photoproduction with number of ψ' particles, Nψ(2S), acceptance, A, photon flux, Φ and the cross section, σ, in different W range.

W (GeV)	<W>	$N_{\psi'}$	A	Φ	σ(Pb)	σ(μb)	Logσ (μb)	Error Logσ(μb)
30-50	40	47	0.107	0.056	1166.6	0.0012	-2.933	± 0.0381
50-70	60	63	0.161	0.034	1745.1	0.0017	-2.758	± 0.0317
70-90	80	71	0.105	0.023	4398.2	0.0044	-2.357	± 0.0202
90-110	100	45	0.130	0.017	3062.4	0.0031	-2.514	± 0.0241
110-130	120	55	0.150	0.013	4277.7	0.0043	-2.369	± 0.0204
130-150	140	70	0.149	0.010	6960.0	0.0070	-2.157	± 0.0162
150-170	160	26	0.117	0.008	4147.9	0.0041	-2.382	± 0.0208

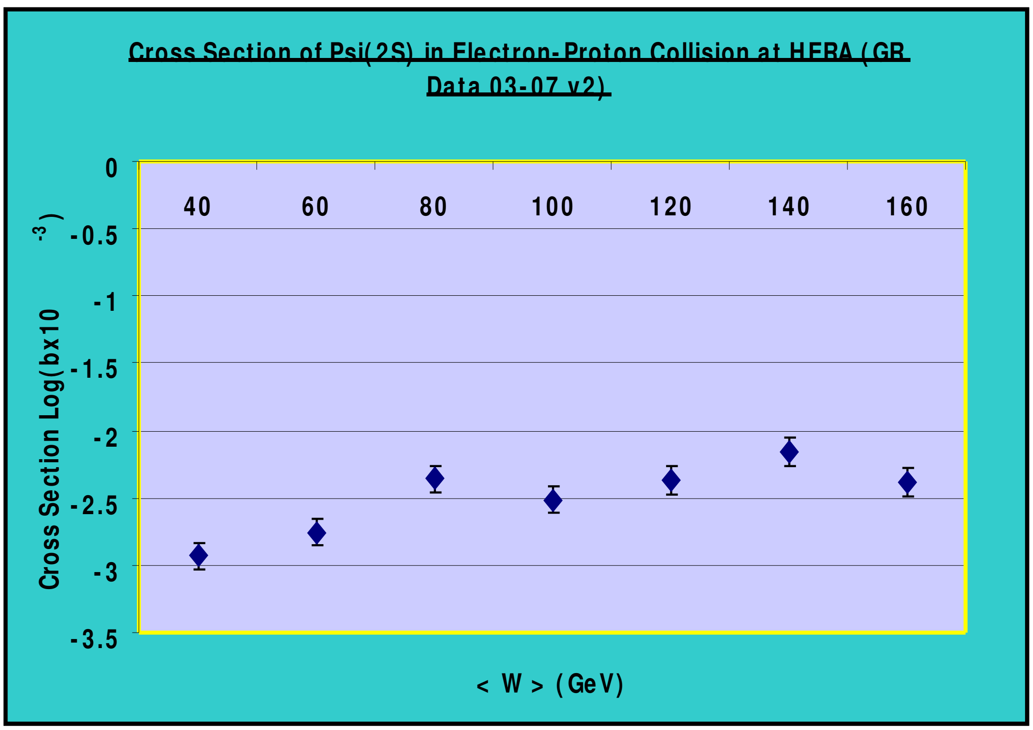

Figure 5.8 : Cross section of ψ' in e-p collision at HERA for ZEUS GR data in 2003-2007 events.

CHAPTER 6

DISCUSSION AND CONCLUSION

In conclusion, ZEUS experiment can be divided into five main aspects. Firstly, we need to understand the physics background which is the main key of the whole experiment. As mentioned in Chapter 1, Standard Model has motivated many physicists to do a lot of researches in particle searching. ZEUS experiment is focusing on the electrons and protons collisions at high energy which is significantly suitable to observe physics events such as photoproduction and deep inelastic scattering. In order to implement that, here comes the second aspect of ZEUS experiment which is the experiment tools; the ZEUS detector and HERA collider. The ZEUS detector consists of two main components; the calorimeter and the tracking detectors. The calorimeter is specially designed to measure the energy of traversing particles, meanwhile the tracking detectors detect the particles tracks as well as measuring the momentum. In measuring the energies and momentum of particles trajectories, ZEUS detector is equipped with many internal computing systems. This is our third aspect. Briefly, there are a lot of routines, files, links, directories, software and programs that had been used in ZEUS experiment. These systems are implemented in detector components, data processing, data simulation, initial selection and many more. In producing raw data from the electrons and protons collisions and extracting it to a better data arrangement, ORANGE is used. The data will then be collected in the form of ntuples. The fourth aspect of ZEUS experiment is the particle offline reconstruction. At this stage, offline selection will be done on the real and simulation data using the analysis software. Lastly, after successfully reconstructing a signal, results are ready for physics analysis and discussions in order to understand the particle behaviours.

As discussion to our results, exclusive photoproduction events are actually compromising specific and narrower region for particle searching in the detector. This is because at initial selection, we have cut off all other events which contribute much bigger percentage in the GR data, such as the DIS and inclusive events. Moreover, in searching for $\psi(2S)$ particle at ZEUS, the specialty of muons as MIPs and specific detector component and system provided in the experiment, leads more convenient searching and facilities for this particle. Muons are easily recognized in the event display by its isolated trajectories which traverse the inner parts of the detector, and reached to the outer layer of where the muon detector is located. After several cut off and event selection, we have seen that the refined distribution of the reconstructed mass before fitting procedure has already shown a remarkable peak.

Our results of $\psi(2S)$ are compared to the production of other VMs in figure 6.1. As a conclusion, we can see that the cross section obtained for $\psi(2S)$ in this research is slightly lower than the H1 results, but is still withim acceptable limits. It is also consistent with the theoretical and parameterization fit given in the graph.

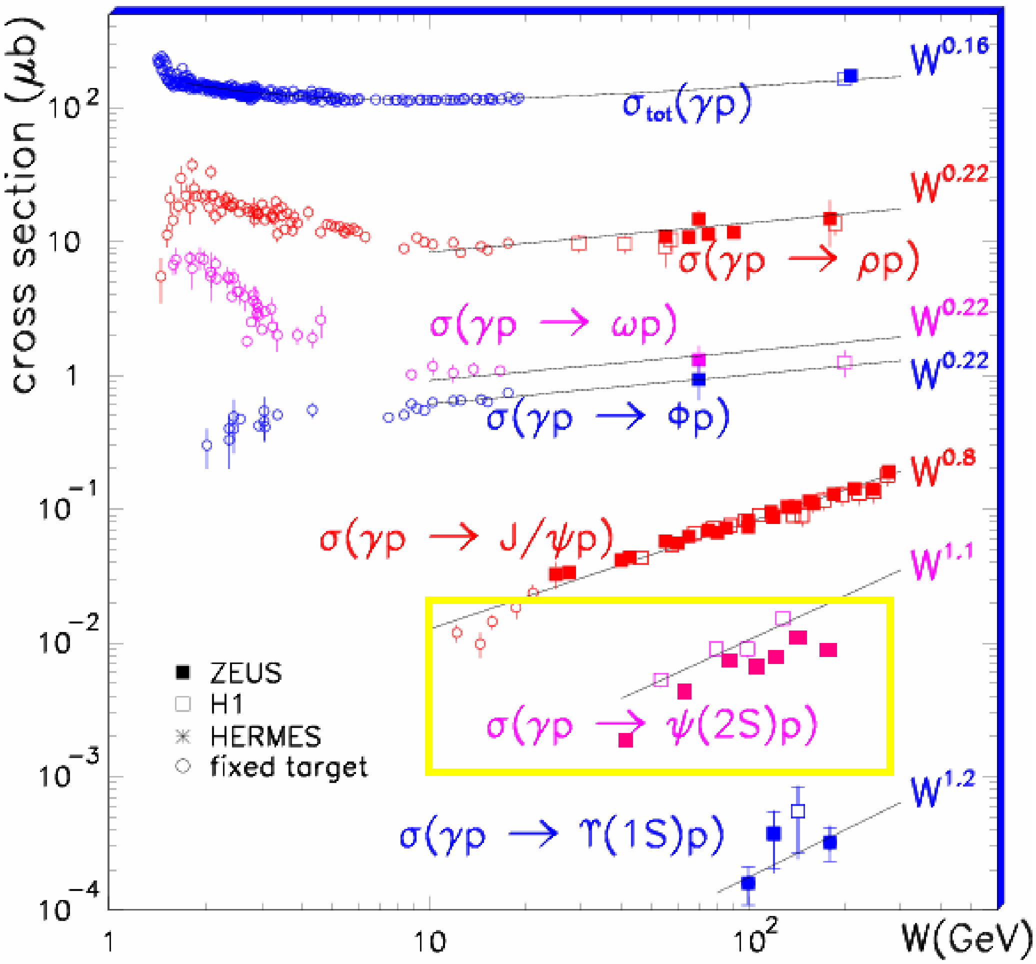

Figure 6.1: The cross section for ψ' at ZEUS highlighted in yellow block, in comparison with H1 experiment and other vector mesons.

Bibliography

[1] P.D.B. Collins, *An Introduction to Regge Theory and High Energy Physics*.Cambridge University Press, England, 1997.

[2] F.J. Hasert et al., Phys.Lett. **46B**, 138 (1973).

[3] M.I. Perl et al., Phys.Rev.Lett **35**, 1489 (1975).

[4] Guang-jiong Ni Guo-hong Yang Rong-tang Fu Haibin Wang, *Running Coupling Constants of Fermions with Masses in Quantum Electro Dynamics and Quantum Chromo Dynamics*, available on http://arxiv.org/abs/hep-ph/9906364v1.

[5] P.D.B. Collins, *An Introduction to Regge Theory and High Energy Physics*. Cambridge University Press, England, 1997.

[6] T. Regge, J.A. Wheeler, Phys. Rev. **108**, 1063 (1957).

[7] A. Donnachie and P.V. Landshoff, Nucl. Phys. **B 231**, 189 (1984).

[8] A. Donnachie and P.V. Landshoff, Phys. Lett. **B 191** (1987).

[9] A. Donnachie and P.V. Landshoff, Phys. Lett. **B 296**, 227 (1992).

[10] V. Barone and E. Predazzi, *High-Energy Particle Diffraction*. Springer, 2002.

[11] J.J. Sakurai, Phys.Rev.Lett **22**, 981 (1969).

[12] R. Ciesielski, *Exclusive J/ψ Production in Deep Inelastic ep Scattering in the ZEUS Experiment at HERA*. Ph.D. Thesis, Faculty of Physics of the Warsaw University, Institute of Experimental Physics, 2004.

[13] M. Seidel. The upgraded interaction regions of HERA. DESY-HERA-00-01.

[14] U. Schneekloth (ed.). The HERA luminosity upgrade. DESY-HERA-98-05.

[15] U. Schneekloth. Recent HERA results and future prospects (1998), hepex/ 9806010.

[16] I.Bloch, *Measurement of Beauty Production from Dimuon Events at HERA/ZEUS*. Ph.D. Thesis, Hamburg University, Hamburg (Germany),

2005. DESY-THESIS-05-034.
[17] ZEUS Collaboration, U. Holm (ed.), *The ZEUS Detector*.
Status Report (unpublished), DESY (1993), available on
http://www-zeus.desy.de/bluebook/bluebook.html.
[18] N. Harnew et al., Nucl. Inst. Meth. **A 279**, 290 (1989).
[19] B. Foster et al., Nucl. Phys. Proc. Suppl. **B 32**, 181 (1993).
[20] B. Foster et al., Nucl. Inst. Meth. **A 338**, 254 (1994).
[21] A. Polini et al., Nucl. Inst. Meth. **A 581**, 31 (2007).
[22] ZEUS Collaboration, U. Holm (ed.), *The ZEUS Detector*.
Status Report (unpublished), DESY (1993), available on
http://www-zeus.desy.de/bluebook/bluebook.html.
[23] I.C. Brock, V. Bashkirov et al.for the ZEUS Collaboration. ZEUS Note
98-046, A Straw-Tube Tracker for ZEUS.
[24] M. Derrick et al., Nucl. Inst. Meth. **A 309**, 77 (1991).
[25] A. Andresen et al., Nucl. Inst. Meth. **A 309**, 101 (1991).
[26] A. Caldwell et al., Nucl. Inst. Meth. **A 321**, 356 (1992).
[27] A. Bernstein et al., Nucl. Inst. Meth. **A 336**, 23 (1993).
[28] B. List and A. Mastroberardino, *DIFFVM - A Monte Carlo Generator*
for Diffractive Processes in ep Scattering., October 16, 1998, available on
https://www.desy.de/~blist/diffvm.html.
[29] D.H. Perkins, *Introduction to High Energy Physics*. Addison-Wesley,
1982.
[30] F. Halzen and A.D. Martin, *Quarks and Leptons: An Introductory Course*
in Modern Particle Physics. John Wiley & Sons, Inc, 1984.
[31] H. Grote, *Review of Pattern Recognition in High Energy Physics*, Reports
on Progress in Physics 50 (1987) 473-500.
[32] H. Albrecht et al., *Search for Rare B Decays*, Phys. Lett. B 353 (1995)
554-562.
[33] ATLAS Collaboration, *ATLAS Inner Detector Technical Design Report*
Vol.I, CERN/LHCC/97-16, CERN (1997).
[34] C. Grupen, *Particle Detectors*, Cambridge Monographs on Particle
Physics, 1996.
[35] D. Green, *The Physics of Particle Detectors*, Cambridge University Press

(2000)

[36] R. Carlin et al. (ZEUS Collaboration), *The ZEUS Microvertex Detector*, Nucl. Instr. and Meth. A511 (2003) 23–37.

[37] R. Mankel, *The HERA-B Experiment: Overview And Concepts*, Proc. International Conference on High-Energy Physics (ICHEP 98), Vancouver 1998 (Canada), Vol. 2, 1513–1518.

[38] H. Wieman et al., *STAR TPC at RHIC*, IEEE Trans. Nucl. Sci. NS-44 (1997) 671–678.

J.H. Thomas, *A TPC for Measuring High Multiplicity Events at RHIC*, Nucl. Instr. and Meth. A478 (2002) 166-169.

M. Anderson et al., *The STAR Time Projection Chamber: a Unique Tool for Studying High Multiplicity Events at RHIC*, Nucl. Instr. and Meth. A499 (2003) 659-678.

[39] R. Fr¨uhwirth, *Application of Kalman Filtering*, Nucl. Instr. and Meth. A262 (1987) 444-450.

[40] P. Billoir, S. Qian, *Simultaneous Pattern Recognition and Track Fitting by the Kalman Filtering Method*, Nucl. Instr. and Meth. A294 (1990) 219-228.

[41] R.H. B¨ock, H. Grote, D. Notz and M. Regler, *Data Analysis Techniques for High-Energy Physics Experiments*, Cambridge Univ. Press (1990). 2nd edition (with R. Fr¨uhwirth) (2000)

[42] main ORANGE web page, http://www-zeus.desy.de/ZEUS_ONLY/analysis/orange/index.html

[43] GMUON web page,

http:// www-zeus.desy.de/~geiser/muon/gmuon.html